北京理工大学

新体系教师岗位升级聘用申请

代表性成果附件材料

姓　　名：黄佳琦

现聘岗位：准聘教授

申请岗位：长聘教授

所在学科：材料科学与工程

所在单位：前沿交叉科学研究院

填表时间：2020 年 4 月 20 日

附件目录

1. **2019 年度科睿唯安高被引科学家（材料科学）**

2. **代表性论文一，金属锂界面离子选择性透过修饰研究 (唯一通讯作者，ESI 高被引论文)。**

   R. Xu#, Y. Xiao#, R. Zhang, X.-B. Cheng, C.-Z. Zhao, X.-Q. Zhang, C. Yan, Q. Zhang, **J.-Q. Huang***. Dual-Phase Single-Ion Pathway Interfaces for Robust Lithium Metal in Working Batteries. ***Adv Mater*** 2019, 31, 1808392.

3. **代表性论文二，金属锂界面调控实现高电压窗口稳定运行研究 (唯一通讯作者，Angew Chem Very Important Paper)**

   C. Yan, R. Xu, J.-L. Qin, H. Yuan, Y. Xiao, L. Xu, **J.-Q. Huang***. 4.5 V High-Voltage Rechargeable Batteries Enabled by the Reduction of Polarization on the Lithium Metal Anode. ***Angew Chem Int Ed*** 2019, 58, 15235.

4. **代表性论文三，锂硫电池界面转化促进机制研究 (唯一通讯作者，ESI 高被引论文)。**

   M. Zhao#, H.-J. Peng#, Z.-W. Zhang, B.-Q. Li, X. Chen, J. Xie, X. Chen, J.-Y. Wei, Q. Zhang, **J.-Q. Huang***. Activating Inert Metallic Compounds for High-Rate Lithium–Sulfur Batteries Through In-Situ Etching of Extrinsic Metal. ***Angew Chem Int Ed*** 2019, 58, 3779.

5. **代表性论文四，金属锂内亥姆霍兹层影响初始固液界面形成和输运特性研究 (唯一通讯作者)**

   C. Yan, H.-R. Li, X. Chen, X.-Q. Zhang, X.-B. Cheng, R. Xu, **J.-Q. Huang***, Q. Zhang. Regulating the Inner Helmholtz Plane for Stable Solid Electrolyte Interphase on Lithium Metal Anodes. ***J Am Chem Soc*** 2019, 141, 9422.

五项代表性成果/奖励

一、 2018、2019 年度科睿唯安高被引科学家（材料科学）

Highly Cited Researcher 2019

presented to

Jia-Qi Huang

in recognition of exceptional research performance demonstrated by production of multiple highly cited papers that rank in the top 1% for field and year in Materials Science

Web of Science Group

Signed Mukhtar Ahmed, President
Date 19 November 2019

A Clarivate Analytics company

五项代表性成果/奖励

二、代表性研究论文，金属锂界面离子选择性透过修饰研究(唯一通讯作者，ESI 高被引论文)。

R. Xu#, Y. Xiao#, R. Zhang, X.-B. Cheng, C.-Z. Zhao, X.-Q. Zhang, C. Yan, Q. Zhang, **J.-Q. Huang***. Dual-Phase Single-Ion Pathway Interfaces for Robust Lithium Metal in Working Batteries. ***Adv Mater*** 2019, 31, 1808392.

ADVANCED MATERIALS
www.advmat.de

Dual-Phase Single-Ion Pathway Interfaces for Robust Lithium Metal in Working Batteries

*Rui Xu, Ye Xiao, Rui Zhang, Xin-Bing Cheng, Chen-Zi Zhao, Xue-Qiang Zhang, Chong Yan, Qiang Zhang, and Jia-Qi Huang**

The lithium (Li) metal anode is confronted by severe interfacial issues that strongly hinder its practical deployment. The unstable interfaces directly induce unfavorable low cycling efficiency, dendritic Li deposition, and even strong safety concerns. An advanced artificial protective layer with single-ion pathways holds great promise for enabling a spatially homogeneous ionic and electric field distribution over Li metal surface, therefore well protecting the Li metal anode during long-term working conditions. Herein, a robust dual-phase artificial interface is constructed, where not only the single-ion-conducting nature, but also high mechanical rigidity and considerable deformability can be fulfilled simultaneously by the rational integration of a garnet Al-doped $Li_{6.75}La_3Zr_{1.75}Ta_{0.25}O_{12}$-based bottom layer and a lithiated Nafion top layer. The as-constructed artificial solid electrolyte interphase is demonstrated to significantly stabilize the repeated cell charging/discharging process via regulating a facile Li-ion transport and a compact Li plating behavior, hence contributing to a higher coulombic efficiency and a considerably enhanced cyclability of lithium metal batteries. This work highlights the significance of rational manipulation of the interfacial properties of a working Li metal anode and affords fresh insights into achieving dendrite-free Li deposition behavior in a working battery.

With the ever-emerging high expectation on energy density from the cutting-edge consumer electronics, electric vehicles, and smart grids, exploring advanced energy storage systems with exceptional high energy density has been strongly considered.[1] Nevertheless, the state-of-the-art lithium-ion batteries (LIBs), approaching a ceiling energy density of 300 Wh kg^{-1}, can no longer catch up with the surgent pursuing trend.[2] Based on a plating/stripping mechanism instead of intercalation chemistry, Li metal anodes possess an extremely high theoretical specific capacity (3860 mAh g^{-1}) and the lowest equilibrium potential (−3.040 V vs standard hydrogen electrode) among various anodes, which holds the promise to be paired with sulfur (S) and oxygen (O_2) cathodes to deliver a three to five times increase in energy density relative to the conventional LIBs.[3]

Attempts to apply Li metal anodes date back to the 1970s. The low cycling efficiency and poor safety issue originating from dendritic Li deposition have placed a huge concern in rechargeable lithium metal batteries (LMBs) since then.[4] To get rid of the intrinsic drawbacks of Li metal anodes and fully suppress the dendrite formation, tremendous investigations have been conducted to probe the Li/electrolyte interphases, the proprieties of which are reported to directly determine Li nucleation and growing patterns.[5]

Generally, the components in nonaqueous liquid electrolyte incline to be reduced by the highly reactive Li metal, resulting in the spontaneous formation of a solid electrolyte interphase (SEI) between the lithium metal and the electrolyte.[6] Nevertheless, the as-formed native SEI is chemically heterogeneous and structurally unstable, which inevitably gives rise to a nonuniform interfacial Li^+ flux and consequently causes the undesirable filament-like Li dendrite growth.[7] Inorganics-rich SEI has been regarded as a more desirable choice to enhance the interfacial stability of Li metal anode considering its high mechanical strength and rapid lithium-ion diffusion pathways.[8] Unfortunately, the brittle inorganics-rich SEI is prone to be ruptured when a huge volume variation is occurred during the repeated plating/stripping of Li metal, which claims the failure of Li metal protection during a long-term cycling.[9] The broken sites with shorter ion transfer pathways become "hot spots" to favor local ion enrichment, thereafter promoting dendrite nucleation and growth.[10] In this consideration, extensive structured hosts have been proposed to alleviate the enormous volume expansion during repeated Li plating/stripping processes to guarantee stable interface,

R. Xu, Y. Xiao, C. Yan, Prof. J.-Q. Huang
School of Materials Science and Engineering
Beijing Institute of Technology
Beijing 100081, China
E-mail: jqhuang@bit.edu.cn
R. Xu, Y. Xiao, C. Yan, Prof. J.-Q. Huang
Advanced Research Institute of Multidisciplinary Science
Beijing Institute of Technology
Beijing 100081, China
R. Zhang, Dr. X.-B. Cheng, C.-Z. Zhao, X.-Q. Zhang, Prof. Q. Zhang
Beijing Key Laboratory of Green Chemical Reaction Engineering and Technology
Department of Chemical Engineering
Tsinghua University
Beijing 100084, China
The ORCID identification number(s) for the author(s) of this article can be found under https://doi.org/10.1002/adma.201808392.

DOI: 10.1002/adma.201808392

which is widely accepted as an effective strategy for developing safe and high-energy-density lithium batteries.[11] For example, sparked reduced graphene oxide was investigated as a Li metal host by Cui and co-workers, which not only provides a stable scaffold for Li plating/stripping, but also contributes to excellent lithiophilicity for uniform Li infusion and deposition.[11f] Actually, if a robust artificial protective interface is enabled with high uniformity, sufficient rigidity, and considerable deformability concurrently, a stabilized Li metal anode can be hopefully expected in the working rechargeable LMBs.[12]

Besides the heterogeneous nature of the SEI, which induces uneven Li-ion transfer, the effects of space charge regions generated by ion depletion on the dendrite proliferation have been highly valued.[13] The dissolved Li salts release mobile Li^+ and anions in routine nonaqueous electrolytes. However, the field-induced transfer of electrochemical active Li^+ with larger solvation cluster is much slower than that of the counterions, which reflects as a low Li-ion transference number (t_{Li^+}, 0.2–0.4) in most liquid electrolytes.[14] The low t_{Li^+} will impose a large Li-ion concentration gradient at the vicinity of Li anode, hence leading to the buildup of a strong interfacial electric field and an exacerbated dendrite propagation (**Figure 1**a). This becomes even more severe under rather high current densities.[15] To this end, emerging electrolytes with high Li-ion transference number are highly pursued and extensively explored during the past decades.[16]

In this contribution, we propose a dual-phase single-ion-conducting artificial interface to protect the Li metal anode in a working battery. A robust inorganics-rich artificial interface can be achieved by rational integration of rigid garnet Al-doped $Li_{6.75}La_3Zr_{1.75}Ta_{0.25}O_{12}$ (LLZTO) and soft lithiated Nafion (Li-Nafion) components. Both garnet-type LLZTO and Li-Nafion were chosen in this work due to their single-ion-conductive nature and high chemical/electrochemical compatibility against Li metal.[17] In details, the garnet Al-doped LLZTO-based bottom layer maintains the high mechanical rigidity and rapid Li^+ transport ability of the protective film,[18] while the Li-Nafion top layer endows the film with considerable elasticity to deform with the volume fluctuation of the electrode. The unique dual-layer LLZTO/Li-Nafion (denoted as LLN) artificial film with nearly unity t_{Li^+} is expected to modulate a homogeneous and high-efficiency Li^+ diffusion manner at the surface of Li anode, subsequently in favor of a compact and dense Li plating pattern (Figure 1b).

The dual-layered LLN coating herein was fabricated via a facile doctor blading method. X-ray diffraction characterization was conducted on the as-prepared LLZTO bottom layer, where a well-maintained cubic phase can be observed (Figure S1, Supporting Information). Note that a small portion (10 wt%) of Li-Nafion as a binder was incorporated in the bottom layer to effectively connect the LLZTO particles and diminish the contact resistance between LLZTO and Li metal.[19] The particle size of LLZTO was determined to be about 66 nm (Figure S2, Supporting Information). The lithiation of Nafion was performed to reduce the Li^+ transfer barrier while enhancing its stability against Li metal, which can be confirmed by the arising peak at around 1630 cm^{-1} in the Fourier transform infrared spectroscopy spectrum, indicating the successful substitution of H^+ by Li^+ (Figure S3, Supporting Information).[20]

The protective layer with dual-layer architecture is composed of a 4 µm thick ceramic bottom layer and a 1 µm thick Li-Nafion top layer according to the cross-sectional scanning electron microscopy (SEM) observation (**Figure 2**a). The top Li-Nafion layer with high uniformity well covered the compact bottom layer from the top-view images and the corresponding element mappings as displayed in Figure S4 (Supporting Information), which equips the LLN film with considerable deformability

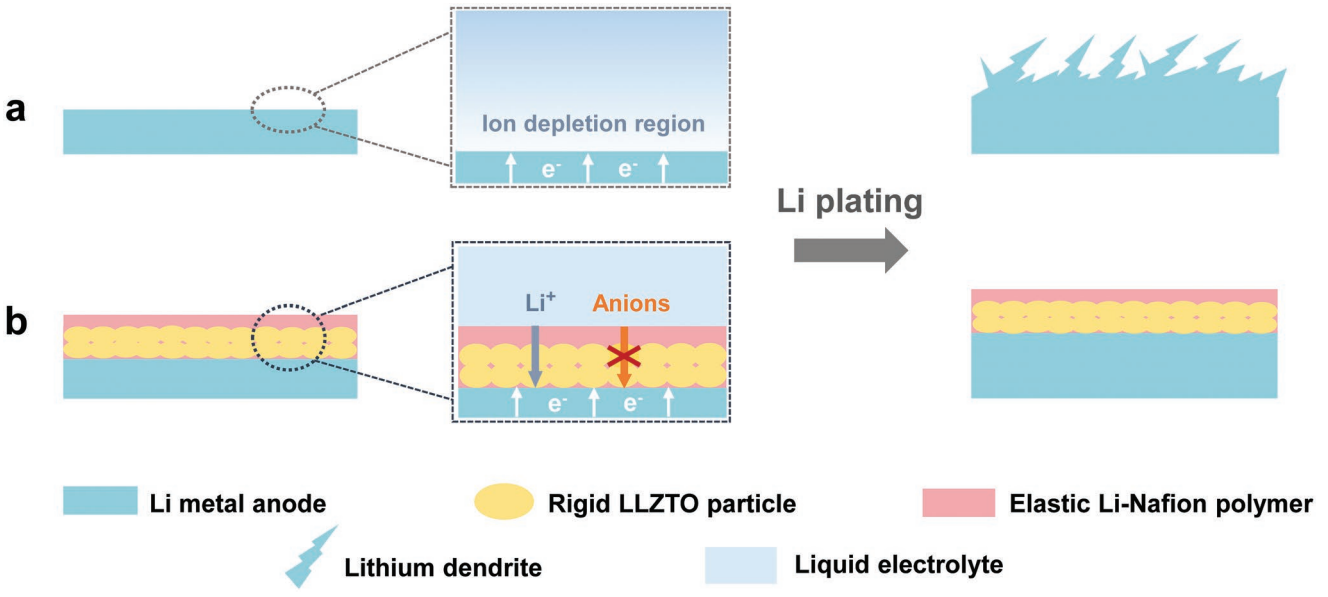

Figure 1. Schematic illustrations of different Li deposition patterns. a) The space charge region induced by anion depletion will impose a strong electric field at the vicinity of bare Li, leading to dendritic Li deposits. b) After incorporating the single-ion-conducting LLN coating composed of rigid LLZTO and elastic Li-Nafion, a uniform and compact Li plating behavior can be obtained.

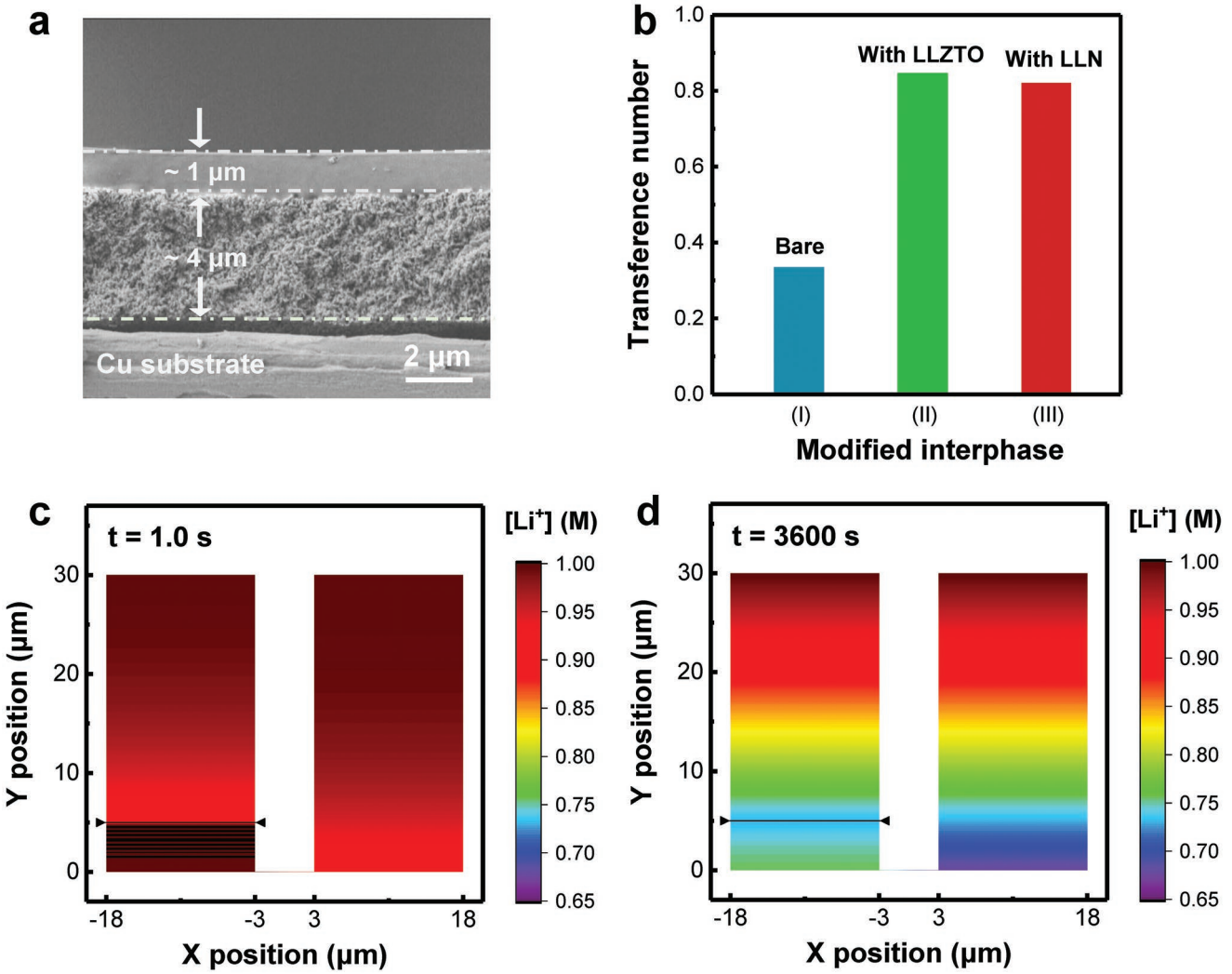

Figure 2. Morphological and ion-transport characterizations of the LLN film. a) Side-view SEM image of the dual-layered LLN with Li-Nafion top layer and LLZTO-based bottom layer. b) A comparison of Li-ion transference number with various modification routes on Li electrodes. c,d) FEM simulation results of Li-ion concentration distribution from bulk electrolyte to anode surface at the initial state (1.0 s) (c) and at a prolonged steady state (3600 s) (d) during the galvanostatic process with (left)/without (right) a 5 μm-thick single-ion-conductive protective film.

to avoid mechanical breakdown during repeated charging/discharging processes.

The ionic conductivity of the LLN protective layer was measured at room temperature using blocking electrode method. A considerable value of 3.0×10^{-5} S cm^{-1} can be determined (Figure S5, Supporting Information), which is slightly lower than individual cubic-phase LLZTO with an ionic conductivity of ≈10^{-4} S cm^{-1} as reported.[21] The t_{Li^+} measurement was further conducted to quantitatively describe the single-ion-conducting ability of the LLN coating layer. In the case of bare symmetric Li cell with conventional carbonate electrolyte (1.0 M $LiPF_6$-EC/DEC, v/v = 1:1), a rather low t_{Li^+} of 0.33 was obtained (Figure S6a, Supporting Information) owing to the faster migration speed of anions than solvated Li^+, which is consistent with previous reports.[22] However, t_{Li^+} can be dramatically improved to 0.82 after the incorporation of LLN coating layer (Figure S6b, Supporting Information). A comprehensive comparison of t_{Li^+} with/without modifications and the related data for the t_{Li^+} determination are listed in Figure 2b and Table S1 (Supporting Information), respectively.

Finite element method (FEM) simulations were carried out to provide insightful understandings on spatial Li-ion concentration distributions when single-ion pathways are present at Li anode surface (Figure 2c,d, and Figure S7 and Movie S1, Supporting Information). In common nonaqueous electrolytes with a low t_{Li^+}, the reverse migration of anions under applied electric field will evidently interfere cation diffusion. As a result, a large Li^+ concentration gradient is generated from bulk electrolyte to anode vicinity after a prolonged galvanostatic process. However, this phenomenon can be considerably alleviated after incorporating a single-ion-conductive protective film. Li ions tend to be attracted to the interface where the immobilization of anion contributes to a more efficient Li^+ transfer mode, replenishing the electrode/electrolyte interface with abundant and homogeneous Li-ion flux.[23] The suppressed ion concentration gradient and uniformized ion

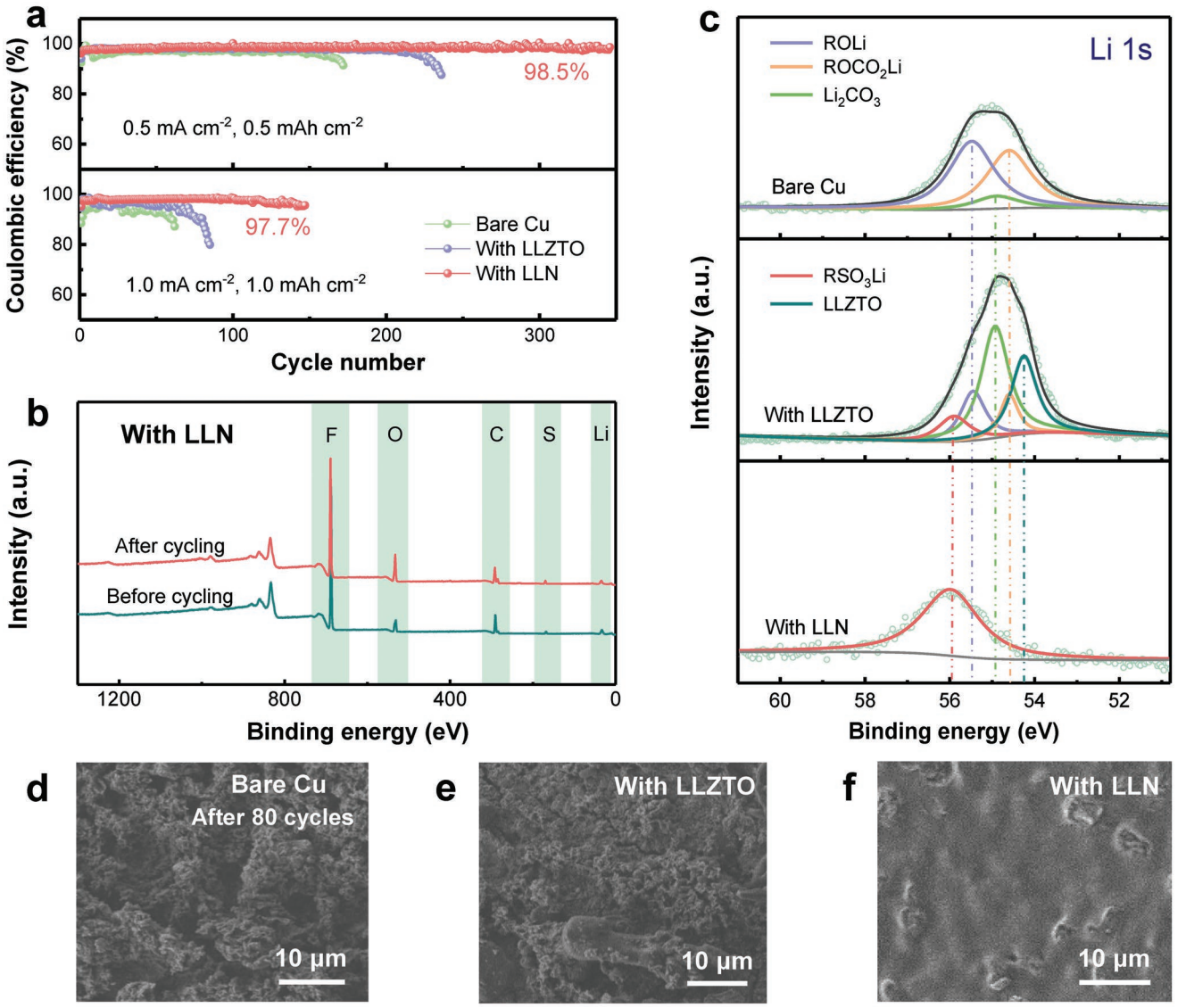

Figure 3. Electrochemical performances of Li | Cu cells. a) Coulombic efficiency of bare Cu, LLZTO-coated Cu, and LLN-coated Cu at various current densities. b) XPS characterizations of LLN-coated Cu before and after 20 cycles at 1.0 mA cm^{-2}, 1.0 mAh cm^{-2}, and c) Li 1s spectrum of the cycled Cu foil with various modifications. d–f) SEM images of bare Cu (d), LLZTO-coated Cu (e), and LLN-coated Cu (f) after 80 cycles at 1.0 mA cm^{-2}, 1.0 mAh cm^{-2}.

distribution are already widely verified to be critical on flat Li plating.[24]

Li | Cu cells are commonly adopted to investigate the cycling efficiency of Li metal anode. The higher coulombic efficiency (CE) and longer lifespan of Li | Cu cells are indictors of a more stable Li plating behavior with more plated Li available for the subsequent stripping. A systematic study was conducted to disclose the effects of interfacial properties on the stability of Li metal by carefully comparing the electrochemical performance of bare Cu, LLZTO-coated Cu, and LLN-coated Cu. Note that the individual LLZTO coating layer can also render a high t_{Li^+} of 0.85 similar to that of LLN coating (Figure S6c, Supporting Information), which is attributed to the unique vacancy Li^+-conducting mechanism in the bulk garnet electrolyte. As shown in **Figure 3**a, the unprotected cell exhibited the worst stability with CE dropping to 91.4% within only 170 cycles at a constant current density of 0.50 mA cm^{-2} and a total Li plating amount of 0.50 mAh cm^{-2}. After the protection of LLZTO, an enhanced performance with an average CE of 97.9% for 220 cycles can be achieved, which is believed to be originated from the optimized Li plating process guaranteed by the combined superiority of LLZTO, i.e., the single-ion-conducting nature as well as high mechanical rigidity.

To confirm this synergistic effect brought by the LLZTO coating, cells modified with sole Li-Nafion soft layer were assembled for comparison, the t_{Li^+} of which was determined to be 0.82 (Figure S8 and Table S1, Supporting Information). There are fluctuant CEs within only 200 cycles (Figure S9, Supporting Information), indicating the significance of the rigidity of LLZTO on the stabilization of Li metal upon long-term cycling. Exclusively, such a stable performance can be dramatically prolonged to more than 350 cycles once modifying

the Cu current collector with the dual-layer LLN coating, where the average CE is determined to be as high as 98.5%. The voltage–time curves are provided in Figure S10 (Supporting Information), which indicate a stable voltage hysteresis of the LLN-protected cell even at the 300th cycle (Figure S9b, Supporting Information).

Furthermore, a Li | Cu cell protected by the LLN coating delivered a stable cycling for over 150 cycles with an average CE of 97.7% when the current density and areal capacity were increased to 1.0 mA cm^{-2} and 1.0 mAh cm^{-2}, respectively. In contrast, the CE of the unprotected cell and LLZTO-protected cell quickly decayed to below 90% within 60 and 80 cycles, respectively. Even at a higher current density of 2.0 mA cm^{-2}, the LLN-protected cell still displayed a decent CE of 95.2% after 80 cycles, far beyond that of the control sample (Figure S11, Supporting Information). Additionally, various dual-phase configurations were also examined in Li | Cu cells, where the configuration composed of LLZTO-based bottom layer and Li-Nafion top layer exhibited the best cell performance over that of the dual-layered film composed of Li-Nafion bottom layer and LLZTO-based top layer as well as the mono-layered LLZTO/Li-Nafion composite film (Figure S12, Supporting Information).

Note that both of LLZTO and LLN coatings are equipped with high Li^+ transference number and superior mechanical strength. To uncover the underlying reasons for such a remarkable performance distinction, post-mortem X-ray photoelectron spectroscopy (XPS) analysis and SEM observations were carried out on the cycled Cu foils with various modifications. As expected, the interfacial composition of LLN-coated Cu maintained consistent before and after cycling (Figure 3b), indicating the superb structural integrity of LLN film during long-term charging/discharging processes. In contrast, the LLZTO-coated Cu displayed a distinctive spectrum after cycling (Figure S13, Supporting Information). In Li 1s spectrum of the LLN-coated Cu, peak only arose at 55.9 eV, which was rationally assigned to the Li^+ containing in Li-Nafion (Figure 3c, bottom), echoing with its S 2s spectrum to confirm that Li-Nafion is the only Li-containing component present on the surface of the cycled LLN-coated Cu (Figure S14, Supporting Information). However, multiple components of RO-Li (55.5 eV), $ROCO_2$-Li (54.6 eV), and Li_2CO_3 (54.9 eV) were detected on the LLZTO-coated Cu besides the original components of LLZTO as well as a limited amount of Li-Nafion binder (Figure 3c, middle). The same components can also be observed on the cycled bare Cu (Figure 3c, top). The corresponding C 1s spectrum of the LLZTO-coated Cu after cycling (Figure S15, Supporting Information) further confirmed the existence of these SEI components.

The morphologies of the modified/unmodified Cu foil after long-term Li plating/stripping were also recorded (Figure 3d–f). Identical loose and porous structure can be observed on the bare Cu (Figure 3d) and LLZTO-coated Cu (Figure 3e), which is regarded as the resistive "dead Li" entangled with thick SEI. Many cracks of the originally compact LLZTO coating can be found after repeated Li plating/stripping processes, exposing fresh Li metal to the nonaqueous electrolytes. The electrolyte consumption and heterogeneous SEI formation occurred at these cracking spots inevitably result in self-amplified dendrite growth, which got disconnected easily from the current collectors during stripping, forming porous "dead Li" just as what occurred on the bare Cu current collectors. However, the LLN-protected Cu displayed a flat and uniform morphology even after 80 cycles under 1.0 mA cm^{-2} (Figure 3f). Such an efficient protection with a superior long-term stability enabled by LLN is derived from its predominant functional advantages of single-ion-conducting nature to render a homogeneous ion flux, and structural merits combining rigid inorganic bottom layer and elastic organic top layer to further physically strengthen the interface while tolerating the volume variation.

Considering that there is heterogeneous nucleation on Cu substrate when Li is plating, which cannot exactly reflect the behavior of Li growth on lithium electrodes, symmetric Li cells are therefore employed to disclose the stability of Li plating/stripping directly on Li substrates. Ultrathin Li electrodes with a thickness of 50 μm were utilized in the following experiments to provide a harsher evaluation in the case of reduced excess Li. The LLN-protected Li exhibited a slightly higher initial polarization of 90 mV (65 mV for bare Li) under the constant current density of 1.0 mA cm^{-2}, which slowly decreased to as low as 45 mV at 100 h, even lower than the initial value of the control sample (**Figure 4**a). This is believed to be as a result of the restrained concentration gradient formation and high-efficiency transport of Li^+ at the interface during long-term cell operation. In contrast, the bare symmetric Li cell displayed a gradual increased polarization to 84 mV at 100 h, finally breaking down within 120 h. Longer galvanostatic time for 3 h was further examined in symmetric Li cell at 1.0 mA cm^{-2}, and a stable polarization of the LLN-protected cell was also obtained as illustrated in Figure S16 (Supporting Information). Even at higher current densities of 2.0 and 3.0 mA cm^{-2}, considerable performance with small polarization (95 and 128 mV, respectively) of the protected cells can be still gained (Figure S17, Supporting Information).

Electrochemical impedance spectroscopy (EIS) was carried out to provide more insights on the cell performance. The real axis intercept of the as-obtained EIS plot represents the bulk resistance of the liquid electrolyte, while the semi-circle is related to the interfacial resistance. As depicted in Figure S18 (Supporting Information), the initial interfacial resistance of both cells decreased due to the higher surface area of the electrode after cycling. Nevertheless, what differs is that the unprotected cell displayed a remarkable growth in bulk resistance after cycling for 100 h (Figure 4b), which is associated with the excessive consumption of liquid electrolyte and the accumulation of thick "dead Li," significantly impeding the bulk transfer of Li^+. However, this phenomenon can be greatly alleviated by incorporating LLN coating layer, where a nearly constant bulk resistance can be observed upon cycling. The conclusions drew in the EIS analysis can be further supported by the distinctive morphology observed on the unprotected (Figure 4c) and LLN-protected Li (Figure 4d) after 100 h cycling. Thick "dead Li" formation is noticed from the side view of the cycled bare Li, in accordance with the polarization augment and fluctuation, whereas the LLN-protected one still remained a relatively compact morphology.

Full cells were assembled for an assessment of the LLN-protection strategy under practical conditions. Ultrathin (50 μm) Li anode, $LiFePO_4$ (LFP) cathode, and conventional carbonate electrolyte of 1.0 M $LiPF_6$-EC/DEC (v:v = 1/1) were

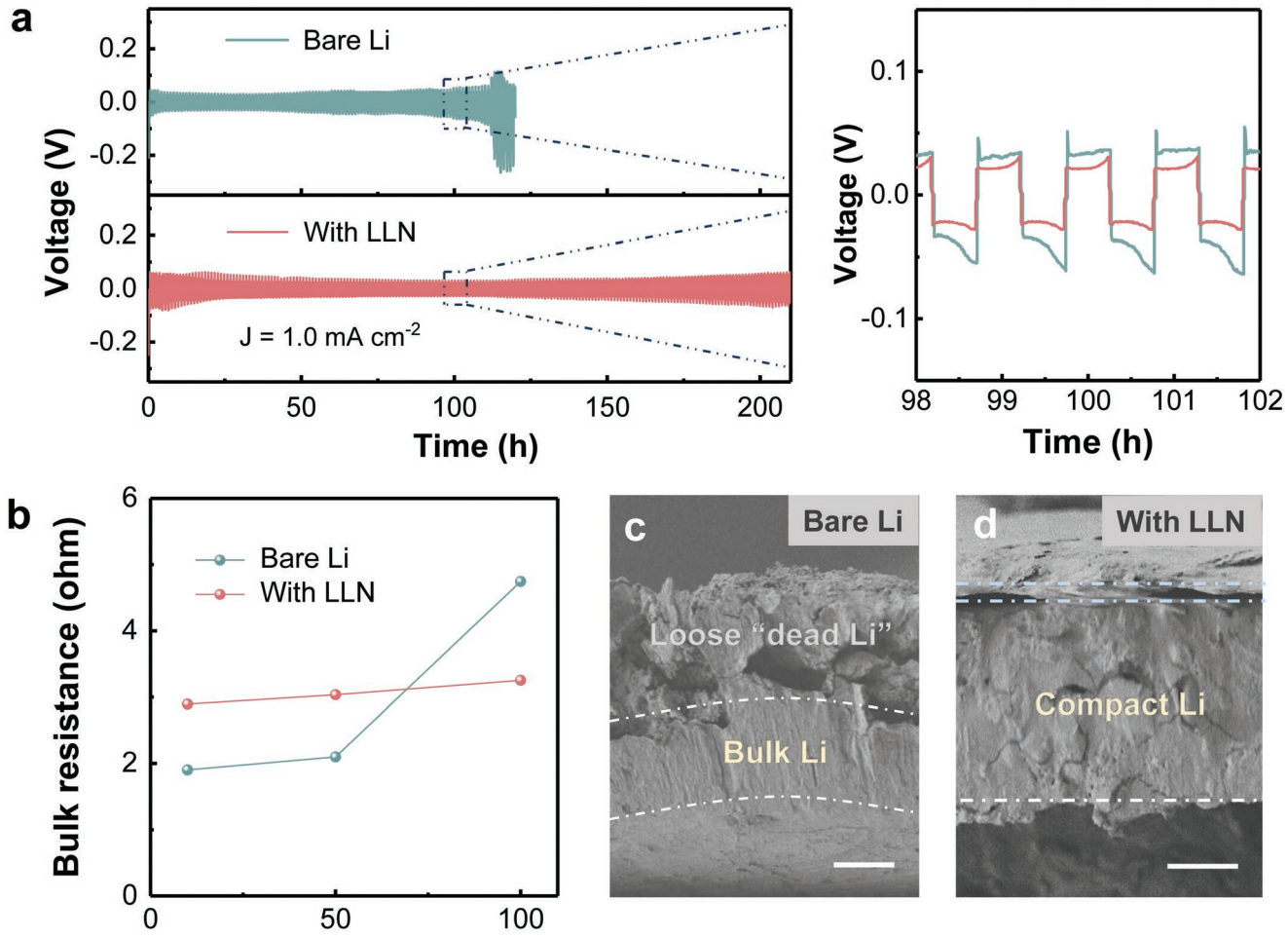

Figure 4. Electrochemical performances of symmetric Li cells with 50 µm thick Li foils. a) Cell performance of bare Li and LLN-coated Li at 1.0 mA cm^{-2}, 0.5 mAh cm^{-2} and the local enlarged voltage–time curve at 100 h. b) The bulk resistance variation after the 10th, 50th, and 100th cycles obtained from equivalent circuit fitting. Side-view SEM images of c) bare Li and d) LLN-coated Li after 100 h cycling, the scale bars of which are 20 µm.

adopted in the cell assembly. As can be seen from **Figure 5**a, the capacity of bare Li began to sharply decline from only 60th cycle at 1 C, which reflects the extremely instability of Li in highly corrosive carbonate electrolyte. However, once disassembling the cycled cell and pairing the cycled cathode with a fresh Li metal, the capacity can recover to 120 mAh g^{-1}, inferring that anode exhaust together with electrolyte consumption is the major factor responsible for the evident capacity fading. The depletion of active Li and liquid electrolyte strongly suggests the unstable electrode/electrolyte interface, which directly induces proliferate parasitic reactions and dendrite growth. In contrast, the LLN-protected Li delivered a significantly more stable cycling with a suppressed capacity decline from 135 to 120 mAh g^{-1} at the 150th cycle, equaling to a capacity retention of 87.4%. This discrepancy on cell degradation can be further explained in the voltage profiles at the and the 100th cycle (Figure 5b), where the voltage polarization of LLN-protected cell increased much more slowly than that of the unprotected cell. This is on account of the well-suppressed electrolyte consumption and "dead Li" accumulation upon cell operation, as has been confirmed in the previous symmetric Li cell tests.

Rate performance was also studied to probe the influence of as-proposed LLN coating on cell capacity (Figure 5c). Initially, the cells with and without LLN protection exhibited nearly the same capacities of 157 (0.1 C) and 156 mAh g^{-1} (0.2 C). However, higher capacities of 148, 135, and 116 mAh g^{-1} were obtained in the case of LLN-protected cell at 0.5, 1, and 2 C, respectively. When resetting to 0.1 C, the cell protected by LLN recovered to a considerable capacity of 158 mAh g^{-1}, a bit higher than the control sample of 155 mAh g^{-1}. The voltage polarizations of the protected/unprotected cells were further investigated (Figure 5d). A slightly larger polarization of 82 mV was observed of the LLN-protected cell comparing to 72 mV of the cell with bare Li at 0.1 C. However, it became comparable to that of the control cell at 0.2 C. Thereafter, the LLN-protected cell displayed a lower polarization (195 mV) than the unprotected one (217 mV) at 0.5 C, and the gap gradually increased with the increasing of the current density. The polarization voltages of 322 mV (protected) versus 386 mV (unprotected) at 1 C and 620 mV (protected) versus 705 mV (unprotected) at 2 C were recorded. The suppressed polarization augment observed upon current increase can be explained from two aspects: (1) The LLN coating is expected to prevent aggressive electrolyte

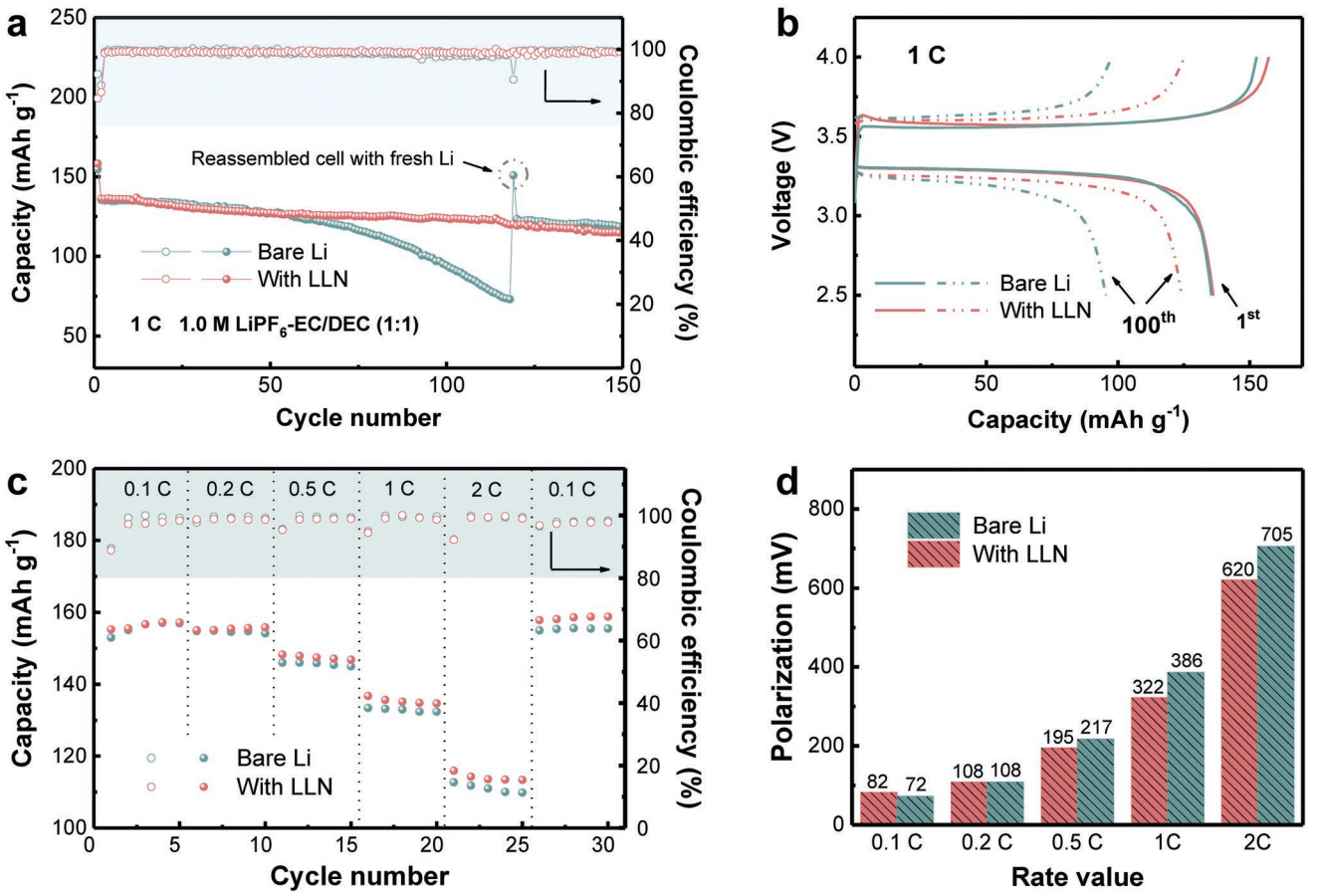

Figure 5. Electrochemical performances of Li | LFP full cells with limited Li excess. a) Specific capacity of Li | LFP cells with bare Li and LLN-coated Li at 1 C rate using conventional carbonate electrolyte; b) the corresponding voltage–capacity curves at the 1st and 100th cycles. c) Rate performance of Li | LFP cells with bare Li and LLN-coated Li at 0.1, 0.2, 0.5, 1, and 2 C; d) a comparison of the corresponding voltage polarizations under various rates.

consumption, therefore minimizing the continuous accumulation of resistive SEI. (2) The suppression of the large Li-ion concentration gradient formation enabled by the single-ion-conductive artificial film is believed to facilitate a facile Li-ion transport at the anode surface even under high current densities.

It is claimed that the strategy of LLN protective film demonstrated herein serves as a proof of concept. It can be further rationally refined as a universal strategy of a dual-layer organic/inorganic hybrid layer, where the organic and inorganic components should meet the standards of: (1) serving as single-ion conductors, (2) endowed with sufficient thermodynamic stability against Li metal, to provide a synergistic protection for working Li metal batteries. Additionally, this strategy of constructing a dual-layer organic/inorganic protective layer can also be potentially extended as a novel capsulation strategy to effectively protect Li metal from the corrosion of air and water, which is urgent and critical for the large-scale deployment of Li metal.

In summary, a robust inorganic-rich artificial interphase with single-ion pathways was proposed to guarantee an efficient protection for Li metal anode during long-term cell operation. Multiple merits have been enabled by this advanced artificial film: (1) Primarily, the single-ion-conducting nature affords a high-efficiency transport and spatially homogeneous distribution of Li-ion at electrode/electrolyte interface as revealed by FEM simulation, which strongly contributes to the subsequent dendrite-free Li plating mode. (2) The dense LLZTO bottom layer with high rigidity is expected to further physically reinforce the Li metal surface via mechanically smoothing the Li deposits. (3) Last but not least, the Li-Nafion top layer enables the interphase with sufficient deformability and robustness to accommodate the volume changes of the electrodes. Therefore, Li | Cu cells protected by LLN delivered a significantly improved average CE of 98.5% for more than 350 cycles, which was greatly higher than that of the unprotected cell (dropping to 91.4% within only 170 cycles). Suppressed augments in bulk resistance and "dead Li" layer thickness during long-term cycling were also observed in the LLN-protected symmetric Li cells. The LLN-protected cell demonstrated a stable cycling with a higher capacity retention of 87.4% after 150 cycles in the practical full cell with ultrathin Li anode and LFP cathode, while the control sample exhibited a sharp capacity decrease from only 60th cycle.

This work elucidates the significance of optimizing the interfacial property on the stabilization of Li metal anode, which is expected to provide a deeper insight on the protection of Li metal. Moreover, this strategy of constructing a rationally designed dual-layer artificial protective layer is also implantable to the interfacial protection of other alkali metal (sodium)-based

battery systems through facilely replacing the Li single-ion conductors with sodium single-ion conductors.

Supporting Information

Supporting Information is available from the Wiley Online Library or from the author.

Acknowledgements

R.X. and Y.X. contributed equally to this work. This work was supported by the National Key Research and Development Program (2016YFA0202500), the National Natural Science Foundation of China (21776019, 21825501, and 21805161), Beijing Natural Science Foundation (L182021), and the Beijing Key Research and Development Plan (Z181100004518001).

Conflict of Interest

The authors declare no conflict of interest.

Keywords

lithium-metal anodes, rechargeable batteries, single-ion pathways, solid electrolyte interphase

Received: December 31, 2018
Revised: February 20, 2019
Published online:

[1] B. Dunn, H. Kamath, J. M. Tarascon, *Science* **2011**, *334*, 928.
[2] M. S. Whittingham, *Chem. Rev.* **2004**, *104*, 4271.
[3] a) Y. Zhu, S. Wang, Z. Miao, Y. Liu, S. L. Chou, *Small* **2018**, *14*, 1801987; b) L. Ma, T. Yu, E. Tzoganakis, K. Amine, T. Wu, Z. Chen, J. Lu, *Adv. Energy Mater.* **2018**, *8*, 1800348; c) Z. W. Zhang, H. J. Peng, M. Zhao, J. Q. Huang, *Adv. Funct. Mater.* **2018**, *28*, 1707536; d) X. Shen, H. Liu, X. B. Cheng, C. Yan, J. Q. Huang, *Energy Storage Mater.* **2018**, *12*, 161.
[4] a) L. Li, S. Li, Y. Lu, *Chem. Commun.* **2018**, *54*, 6648; b) W. Xu, J. Wang, F. Ding, X. Chen, E. Nasybutin, Y. Zhang, J. G. Zhang, *Energy Environ. Sci.* **2014**, *7*, 513.
[5] a) M. D. Tikekar, S. Choudhury, Z. Tu, L. A. Archer, *Nat. Energy* **2016**, *1*, 16114; b) X. Yu, A. Manthiram, *Energy Environ. Sci.* **2018**, *11*, 527; c) X. B. Cheng, C. Yan, X. Q. Zhang, H. Liu, Q. Zhang, *ACS Energy Lett.* **2018**, *3*, 1564; d) K. Xu, *Chem. Rev.* **2014**, *114*, 11503; e) X. Fan, L. Chen, O. Borodin, X. Ji, J. Chen, S. Hou, T. Deng, J. Zheng, C. Yang, S.-C. Liou, K. Amine, K. Xu, C. Wang, *Nat. Nanotechnol.* **2018**, *13*, 715.
[6] a) J. B. Goodenough, Y. Kim, *Chem. Mater.* **2010**, *22*, 587; b) D. Aurbach, A. Zaban, Y. Gofer, Y. Ein-Ely, I. Weissman, O. Chusid, O. Abramson, *J. Power Sources* **1995**, *54*, 76.
[7] a) S. Wei, S. Choudhury, Z. Tu, K. Zhang, L. A. Archer, *Acc. Chem. Res.* **2018**, *51*, 80; b) D. Aurbach, Y. Gofer, J. Langzam, *J. Electrochem. Soc.* **1989**, *136*, 3198; c) Y. Li, Y. Li, A. Pei, K. Yan, Y. Sun, C. L. Wu, L. M. Joubert, R. Chin, A. L. Koh, Y. Yu, J. Perrino, B. Butz, S. Chu, Y. Cui, *Science* **2017**, *358*, 506.
[8] a) C. Wang, Y. S. Meng, K. Xu, *J. Electrochem. Soc.* **2019**, *166*, A5184; b) N. W. Li, Y. X. Yin, C. P. Yang, Y. G. Guo, *Adv. Mater.* **2016**, *28*, 1853; c) Q. Pang, L. Zhou, L. F. Nazar, *Proc. Natl. Acad. Sci. USA* **2018**, *115*, 5343; d) Y. Yuan, F. Wu, Y. Bai, Y. Li, G. Chen, Z. Wang, C. Wu, *Energy Storage Mater.* **2019**, *16*, 411.
[9] a) N. W. Li, Y. Shi, Y. X. Yin, X. X. Zeng, J. Y. Li, C. J. Li, L. J. Wan, R. Wen, Y. G. Guo, *Angew. Chem., Int. Ed.* **2018**, *57*, 1505; b) R. Xu, X. Q. Zhang, X. B. Cheng, H. J. Peng, C. Z. Zhao, C. Yan, J. Q. Huang, *Adv. Funct. Mater.* **2018**, *28*, 1705838; c) F. Wu, Y. X. Yuan, X. B. Cheng, Y. Bai, Y. Li, C. Wu, Q. Zhang, *Energy Storage Mater.* **2018**, *15*, 148.
[10] A. Kushimaa, K. P. So, C. Su, P. Bai, N. Kuriyamac, T. Maebashi, Y. Fujiwara, M. Z. Bazant, J. Li, *Nano Energy* **2017**, *32*, 271.
[11] a) Z. Sun, S. Jin, H. Jin, Z. Du, Y. Zhu, A. Cao, H. Ji, L. J. Wan, *Adv. Mater.* **2018**, *30*, 1800884; b) R. Zhang, N. W. Li, X. B. Cheng, Y. X. Yin, Q. Zhang, Y. G. Guo, *Adv. Sci.* **2017**, *4*, 1600445; c) L. Liu, Y. X. Yin, J. Y. Li, N. W. Li, X. X. Zeng, H. Ye, Y. G. Guo, L. J. Wan, *Joule* **2017**, *1*, 563; d) R. Zhang, X. Chen, X. Shen, X. Q. Zhang, X. R. Chen, X. B. Cheng, C. Yan, C. Z. Zhao, Q. Zhang, *Joule* **2018**, *2*, 764; e) C. Yang, Y. Yao, S. He, H. Xie, E. Hitz, L. Hu, *Adv. Mater.* **2017**, *29*, 1702714; f) D. Lin, Y. Liu, Z. Liang, H. W. Lee, J. Sun, H. Wang, K. Yan, J. Xie, Y. Cui, *Nat. Nanotechnol.* **2016**, *11*, 626.
[12] a) X. Q. Zhang, X. B. Cheng, Q. Zhang, *Adv. Mater. Interfaces* **2018**, *5*, 1701097; b) Y. Liu, D. Lin, P. Y. Yuen, K. Liu, J. Xie, R. H. Dauskardt, Y. Cui, *Adv. Mater.* **2017**, *29*, 1605531.
[13] J. N. Chazalviel, *Phys. Rev. A* **1990**, *42*, 7355.
[14] Z. Tu, S. Choudhury, M. J. Zachman, S. Wei, K. Zhang, L. F. Kourkoutis, L. A. Archer, *Joule* **2017**, *1*, 394.
[15] C. Brissot, M. Rosso, J. N. Chazalviel, S. Lascaud, *J. Power Sources* **1999**, *81–82*, 925.
[16] a) R. Bouchet, S. Maria, R. Meziane, A. Aboulaich, L. Lienafa, J. P. Bonnet, T. N. T. Phan, D. Bertin, D. Gigmes, D. Devaux, R. Denoyel, M. Armand, *Nat. Mater.* **2013**, *12*, 452; b) Y. Lu, M. Tikekar, R. Mohanty, K. Hendrickson, L. Ma, L. A. Archer, *Adv. Energy Mater.* **2015**, *5*, 1402073; c) C. Z. Zhao, X. Q. Zhang, X. B. Cheng, R. Zhang, R. Xu, P. Y. Chen, H. J. Peng, J. Q. Huang, Q. Zhang, *Proc. Natl. Acad. Sci. USA* **2017**, *114*, 11069; d) Z. Tu, P. Nath, Y. Lu, M. D. Tikekar, L. A. Archer, *Acc. Chem. Res.* **2015**, *48*, 2947.
[17] a) K. K. F. Fu, Y. G. Gong, B. L. Liu, Y. Zhu, S. Xu, Y. Yao, W. Luo, C. Wang, S. D. Lacey, J. Dai, Y. Chen, Y. Mo, E. Wachsman, L. Hu, *Sci. Adv.* **2017**, *3*, e1601659; b) J. Xiang, Y. Zhao, L. Yuan, C. Chen, Y. Shen, F. Hu, Z. Hao, J. Liu, B. Xu, Y. Huang, *Nano Energy* **2017**, *42*, 262.
[18] V. Thangadurai, S. Narayanan, D. Pinzaru, *Chem. Soc. Rev.* **2014**, *43*, 4714.
[19] Y. Li, B. Xu, H. Xu, H. Duan, X. Lu, S. Xin, W. Zhou, L. Xue, G. Fu, A. Manthiram, J. B. Goodenough, *Angew. Chem., Int. Ed.* **2017**, *56*, 753.
[20] J. Gao, C. Sun, L. Xu, J. Chen, C. Wang, D. Guo, H. Chen, *J. Power Sources* **2018**, *382*, 179.
[21] R. Murugan, V. Thangadurai, W. Weppner, *Angew. Chem., Int. Ed.* **2007**, *46*, 7778.
[22] X. Mao, L. Shi, H. Zhang, Z. Wang, J. Zhu, Z. Qiu, Y. Zhao, M. Zhang, S. Yuan, *J. Power Sources* **2017**, *342*, 816.
[23] a) M. D. Tikekar, L. A. Archer, D. L. Koch, *Sci. Adv.* **2016**, *2*, e1600320; b) Q. Pang, X. Liang, A. Shyamsunder, L. F. Nazar, *Joule* **2017**, *1*, 871.
[24] a) W. Liu, D. Lin, A. Pei, Y. Cui, *J. Am. Chem. Soc.* **2016**, *138*, 15443; b) X. B. Cheng, T. Z. Hou, R. Zhang, H. J. Peng, C. Z. Zhao, J. Q. Huang, Q. Zhang, *Adv. Mater.* **2016**, *28*, 2888; c) W. Zhang, H. L. Zhuang, L. Fan, L. Gao, Y. Lu, *Sci. Adv.* **2018**, *4*, eaar4410.

五项代表性成果/奖励

三、代表性研究论文，金属锂界面调控实现高电压窗口稳定运行研究

(唯一通讯作者，Angew Chem, Very Important Paper)

C. Yan, R. Xu, J.-L. Qin, H. Yuan, Y. Xiao, L. Xu, **J.-Q. Huang***. 4.5 V High-Voltage Rechargeable Batteries Enabled by the Reduction of Polarization on the Lithium Metal Anode. ***Angew Chem Int Ed*** 2019, 58, 15235.

VIP High-Voltage Batteries Very Important Paper

International Edition: DOI: 10.1002/anie.201908874
German Edition: DOI: 10.1002/ange.201908874

4.5 V High-Voltage Rechargeable Batteries Enabled by the Reduction of Polarization on the Lithium Metal Anode

*Chong Yan, Rui Xu, Jin-Lei Qin, Hong Yuan, Ye Xiao, Lei Xu, and Jia-Qi Huang**

Abstract: *Lithium metal is used to achieve high-energy-density batteries due to its large theoretical capacity and low negative electrochemical potential. The introduction of quasi-solid electrolytes simultaneously overcomes the safety problems induced by the liquid electrolytes and the high interfacial resistance issues confronted by all solid-state electrolytes. In-depth investigations involving interfacial behaviors in quasi-solid lithium metal batteries are inadequate. Herein an ultra-thin Li_3OCl quasi-solid-state electrolyte layer (500 nm thickness) is used to cover a lithium anode. The polarization of the anode is remarkably reduced by introducing the Li_3OCl quasi-solid-state electrolyte. In contrast to the decomposition of solvents in a standard electrolyte (EC-DEC,1.0 M $LiPF_6$), the established quasi-solid-state electrolyte interfaces can significantly inhibit the decomposition of solvents when the cut-off voltage is 4.5 V.*

Since 1913 lithium metal has been considered as the "Holy Grail" of anodes in rechargeable batteries owing to its high theoretical capacity (3860 $mAh\,g^{-1}$) and the lowest negative electrochemical potential (−3.04 V vs. standard hydrogen electrode).[1] However, the slow progress of research on lithium metal regarding safety issues in liquid electrolytes seriously hinders its practical application.[2] The investigations on lithium-metal batteries have stagnated due to the applications of graphite anodes.[3] Fortunately, the lithium anode has been revived as a result of the urgent demand for higher-energy-density energy storage systems.[4,5] Research focusing on solid-state electrolytes simultaneously has been strongly considered[6–8] because: 1. The high melting point of solid-state electrolytes enable the battery to work normally, while it induces the combustion of the vaporized organic electrolyte in routine Li ion batteries.[9] 2. Most of the solid-state electrolytes exhibit a wide electrochemical window and are employed to match high-voltage (higher than 4.3 V) cathodes.[10] 3. The good environmental compatibility between Li electrodes and most solid-state electrolytes ensures the formation of stable interfaces, drastically reducing the continuous consumption of electrolytes. Actually, when matching with Li anode alone, there are notorious contact issues during cycling for either organic polymer electrolytes or inorganic ceramic electrolytes.[8,11] Therefore, there is always a high interfacial resistance in all-solid-state-electrolyte batteries that hinders the demonstration of high-voltage rechargeable batteries.

Extensive efforts have been devoted to reduce the interfacial resistance.[5,12] The addition of a small amount of liquid electrolyte to solid-state electrolytes was proved as an effective method.[13] The intermediate state (mass fraction of liquid lower than 5 wt% in the composite electrolyte) between solid and liquid is denoted as the quasi-solid-state. However, the mechanism on the quasi-solid-state electrolyte interface has not been covered yet. How to distinguish the potential in two-electrode cells is an open question. A clear scenario is required to describe potential changes during charge and discharge in lithium metal systems with both routine electrolyte and quasi-solid-state electrolyte. Consequently, precisely monitoring the potential of the lithium electrode is urgently needed to probe the interfacial behavior and understand the energy chemistry at the working interfaces.

In this contribution, a 4.5 V high-voltage rechargeable battery is enabled by the reduction of polarization on a lithium metal anode. Herein a 500-nm-thick antiperovskite Li_3OCl layer is coated on the surface of a lithium anode and the cathode is wetted with a lean electrolyte (0.8 μL per gram of cathode active materials) in a 4.5 V lithium metal battery. The interfacial behavior of the quasi-solid-state electrolyte is monitored by a three-electrode measurement. We propose that the quasi-solid-state electrolyte can stabilize the interfaces to achieve a high utilization rate of lithium and effectively reduce the polarization of lithium metal electrode (Figure 1). The quasi-solid-state interphase can render a high Gibbs free energy for electrochemical oxidation of electrolyte interphases and broaden the redox window of liquid electrolyte,[7] leading to a Li chemical potential of the cathode electrolyte interphase (CEI)/liquid electrolyte interface that is higher than the oxidation limit of liquid electrolyte.[14] Consequently, the decomposition of liquid electrolyte is remarkably inhibited, leading to high average Coulombic efficiency and high capacity retention rate in a 4.5 V high-voltage lithium metal battery.

The nonflammable, thickness-controllable, and light-weight features make Li_3OCl[15] a potential alternative for the realization of safe and high-energy-density batteries. The synthesis and detailed related features are described in Figures S1 and S2. The spherical particles of Li_3OCl are approximately 50 nm in diameter (Figure 1 a), ensuring dense stacking in the formation of a uniform protective layer. The

[*] C. Yan, R. Xu, J.-L. Qin, Y. Xiao, L. Xu, Prof. J.-Q. Huang
School of Materials Science and Engineering
Beijing Institute of Technology, Beijing 100081 (P. R. China)
E-mail: jqhuang@bit.edu.cn
C. Yan, R. Xu, J.-L. Qin, Dr. H. Yuan, Y. Xiao, L. Xu, Prof. J.-Q. Huang
Advanced Research Institute of Multidisciplinary Science
Beijing Institute of Technology, Beijing 100081 (P. R. China)
Supporting information and the ORCID identification number(s) for the author(s) of this article can be found under: https://doi.org/10.1002/anie.201908874.

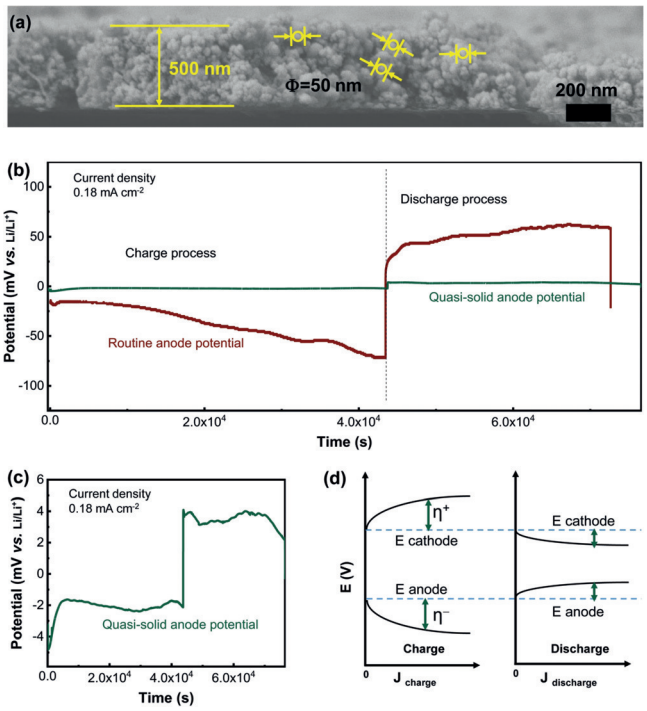

Figure 1. a) The morphology of the Li_3OCl ultrathin solid-state electrolyte layer . b,c) Anode potential profiles in the quasi-solid and routine electrolyte, obtained in three-electrode configuration, the current density is 0.18 mA cm^{-2}. d) Correlation between presented potential and current density in the charge/discharge process.

orderly stacked Li_3OCl nanoparticles effectively transport lithium ions and inhibit the growth of lithium dendrites due to the high ionic conductivity and high Young's modulus, respectively. Besides, the unoccupied space between spherical particles in the Li_3OCl layer is filled with liquid electrolyte and lithium salts, allowing rapid diffusion of lithium ions. The transfer number of Li ions in the quasi-solid-state electrolyte is 0.67 (Figure S3), well above the value of 0.34 in routine electrolyte (volume ratio of ethylene carbonate (EC):diethyl carbonate (DEC) is 1:1, 1.0 M $LiPF_6$),[16] indicating the anions with large radius are significantly immobilized.

A three-electrode device was specially customized to precisely record the potential of the anode in a working cell. The schematic diagram of the three-electrode system is exhibited in Figure S4. The three electrodes consist of lithium foil (working electrode), lithium string (reference electrode), and a $LiNi_{0.85}Co_{0.1}Al_{0.05}O_2$ (NCA) plate (counter electrode). As a result, the overpotential was only 2 mV in quasi-solid-state electrolyte; in contrast the overpotential of the anode was 50 mV in routine electrolyte at a current density of 0.18 mA cm^{-2} (rate = 0.2 C), (Figure 1 b,c). The 50 mV overpotential was consistent with Winter's report,[17] in which 50 mV is determined at 0.12 mA cm^{-2}. Note that when the electrochemical processes occur in a battery, the potentials of both the cathode and anode deviate away from the equilibrium potential. There is a positive correlation between the presented potential and the current density (Figure 1 d). The polarization of the anode induced by the quasi-solid-state electrolyte is sharply reduced, efficiently stabilizing the interphases and enhancing the ion transport in the solid electrolyte interphase (SEI) layer.

Cyclic voltammetry (CV) and linear sweep voltammetry (LSV) were applied to probe the details of the electrochemical behavior. The cells exhibit a typical oxidation peak when the positive scan was recorded at a scan rate of 0.1 mV s^{-1}. However, when the scanning voltage of the cells was above 4.46 V, the routine electrolyte started to decompose, resulting in erratic negative scan curves (Figure 2 a). The

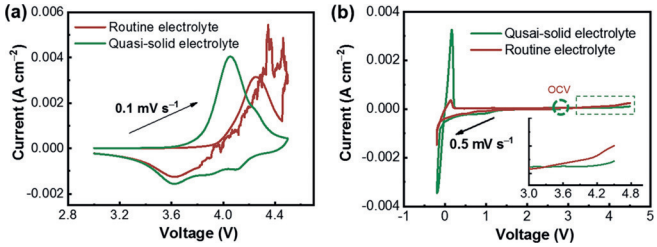

Figure 2. Electrochemical behavior of the routine and quasi-solid state electrolytes. a) Redox behavior tested with cyclic voltammetry, the scan rate is 0.1 mV s^{-1}; b) Potential window of electrolyte tested with linear sweep voltammetry, the scan rate is 0.5 mV s^{-1}.

quasi-solid-state electrolyte renders a stable redox reaction even when the voltage is above 4.5 V. The electrochemical behavior remains constant in successive CV scans (Figure S5). The following LSV results are also consistent with the CV profiles. The response current exhibits a sharp increase when the scanning voltage is over 4.5 V in routine electrolyte, while this does not happen in quasi-solid-state electrolyte (Figure 2 b).

It has been widely accepted that the practical potential of an electrode has contributions from the thermodynamic electrode potential, electrochemical polarization, concentration polarization, and ohmic polarization. Since the current density of the Li anode was the same in both cells, the thermodynamic electrode potential (0 V vs. Li/Li$^+$) and electrochemical polarization contribute little, indicting the main factor is concentration polarization and ohmic polarization. There is a quasi-solid-state electrolyte that regulates the Li ion concentration covered on the lithium surface. This favors the rapid transport of Li ions, further reducing the concentration polarization and ohmic polarization. Therefore, the quasi-solid-state interphase with high ionic conductivity renders the high Gibbs free energy of the electrochemical oxidation of the electrolyte interphase and broadens the redox window of the liquid electrolyte.[7] As a result, the Li chemical potential of CEI/liquid electrolyte interface is higher than the oxidation limit of the liquid electrolyte,[14] and solvent molecules are in an integrated state in the quasi-solid-state electrolyte cell.Correspondingly, the solvent molecules decomposed in a routine electrolyte cell.

The quasi-solid-state electrolyte was applied in Li metal batteries to explore its electrochemical performance. When a pristine lithium anode was matched with an NCA cathode (Figure S6), improved battery performance was achieved with the employment of Li_3OCl layer even at lean electrolyte conditions (0.8 μL per gram of cathode active materials). As

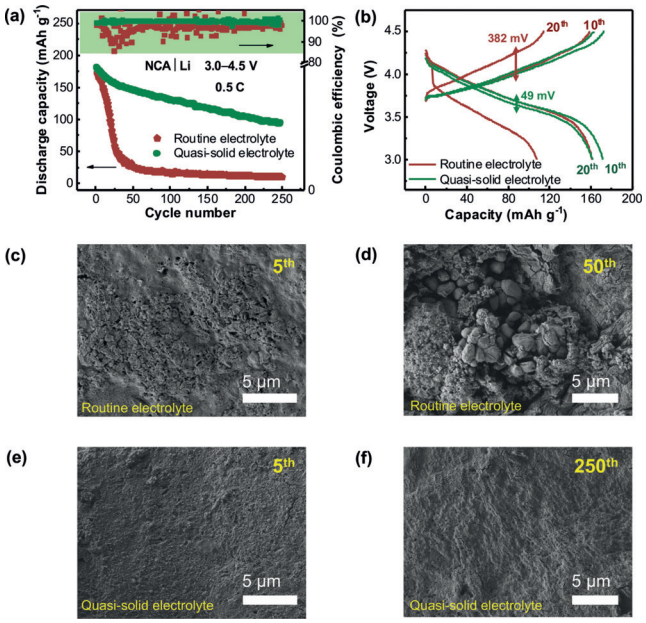

Figure 3. Electrochemical performance of NCA | Li batteries and morphology evolution of the lithium anode during cycles. a) The discharge capacity and Coulombic efficiency curves in routine and quasi-solid electrolytes, charge/discharge rate is 0.5 C and the voltage windows is 3.0–4.5 V. b) Polarization voltage for different cycles. c,d) Morphology of the lithium anode after the 5th and 50th cycle in routine electrolyte, large amounts of inactive lithium is generated. e,f) Morphology of the lithium anode after the 5th and 250th cycle in quasi-solid electrolyte, exhibiting smooth and integrated morphology.

shown in Figure 3a, the capacity of the battery without the Li_3OCl layer decreases rapidly, the Coulombic efficiency is seriously fluctuant, and the capacity even reduces to near 0 mAh g^{-1} after only 50 cycles at 0.5 C. In contrast, the discharge capacity of a lithium battery with 500-nm-thick Li_3OCl layer (areal loading amount of 0.11 mg cm^{-2}) stays at 100 mAh g^{-1} after 250 cycles and an average Coulombic efficiency of up to 99.7%, exhibiting a better capacity retention and higher Coulombic efficiency. The capacity–voltage profiles imply the constant overpotential during the evolution of cycling. There is only approximately 49 mV hysteresis voltage after 20 cycles, while the overpotential in routine electrolyte is up to 382 mV (Figure 3b), indicating the quasi-solid-state electrolyte renders the rapid transport of Li ions during repeated cycles. According to SEM images of the Li anode after the fifth cycle and long-term cycling (Figure 3c–f), the pristine Li exhibits cracks and mossy dendrites while the protected lithium exhibits a smooth morphology, indicating the highly reactive Li anode has been well protected in a working cell. In addition, electrochemical impedance spectroscopy profiles both before and after cycling exhibit reduced interfacial resistance and charge transfer resistance in the quasi-solid-state electrolyte than those with routine electrolytes (Figures S7 and S8). The products of decomposition and formation of inactive Li dendrites in routine electrolyte covered on electrodes obviously increase the interfacial resistance of the working battery. Therefore, the application of a Li_3OCl layer results in long-term cycling and low resistance in the quasi-solid-state electrolyte NCA | Li battery. This corresponds to the conclusion that the quasi-solid-state interphase renders the rapid transport of Li ions.

X-ray photoelectron spectroscopy (XPS) was further applied to detect the evolution of the chemical composition (Figure S9). In the Li 1s XPS spectrum, the main characteristic peaks related to Li-O (54.04 eV), Li-OH (54.42 eV), and Li-Cl (54.87 eV) always appeared and no additional peaks were observed during cycling. The bulk characteristic peaks of Li_3OCl (197.39 eV for Cl $2p_{3/2}$, 199.19 eV for Cl $2p_{1/2}$) are still observed and LiCl (198.2 eV for Li-Cl $2p_{3/2}$, 198.8 eV for Li-Cl $2p_{1/2}$) is generated after the tenth cycle according to the Cl 2p XPS spectrum, indicating interfacial Li_3OCl is transformed into LiCl to form a halogenated layer, which is consistent with Liang's report.[18]

Generally, the cut-off voltage of the NCA | Li battery was 4.3 V in order to achieve stable and long-term cycling, and the structure of cathode materials and the solvents in electrolyte was kept stable. When the NCA | Li battery was cycled at a range of 3.0–4.5 V or higher and no other high-voltage additive was introduced to the electrolyte, the liquid electrolyte usually suffers from serious decomposition (Figure 4a). In Li_3OCl quasi-solid-state electrolyte, the polarization of lithium metal anode is significantly reduced, indicating rapid transport of Li ions through the SEI layer. The lower overpotential of anode renders a high Gibbs free energy of electrochemical oxidation of the electrolyte interphase,[7] leading to a large operating voltage window of the solvent molecules (Figure 4b). Therefore, the employment of quasi-solid-state ceramic interfaces benefits the long-term cycling in 4.5 V high-voltage lithium metal batteries.

In summary, high average Coulombic efficiency and a high capacity retention rate in a 4.5 V high-voltage lithium metal battery were achieved by introduction of lightweight antiperovskite solid-state electrolyte Li_3OCl on lithium metal anode with a lean amount of liquid electrolyte. Compared to an all-solid-state electrolyte battery, the application of small amount of liquid electrolyte (mass fraction of liquid lower than 5 wt.%) has significantly improved interfacial contacts between electrolytes and electrodes simultaneously, resulting in an integrated buffer layer. The overpotential of lithium

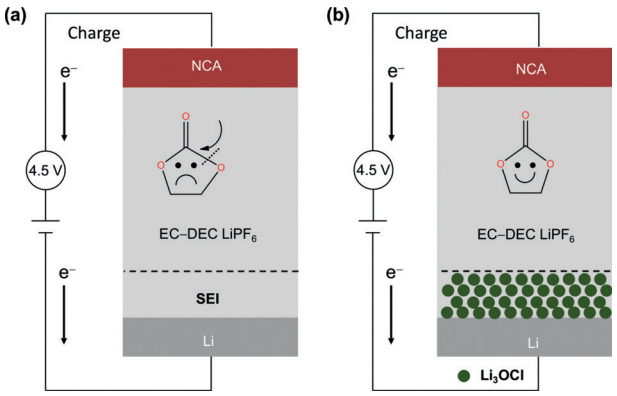

Figure 4. Schematic of the influence of the reduced polarization on lithium metal anode. a) The solvent molecules in routine electrolyte decompose under 4.5 V high-voltage conditions. b) The Li_3OCl quasi-solid electrolyte layer that covers the lithium metal efficiently prohibits the decomposition of solvent molecules.

metal electrode was significantly reduced and the decomposition of solvent molecules was markedly inhibited. In addition, the quasi-solid-state ceramic interfaces also reduce the polarization of lithium metal anode and enhance the ion transport. The fresh understanding about quasi-solid-state interface can enrich the knowledge about interfacial chemistry, which affords valuable references to achieve a better quasi-solid-state interface and realize longer life-span lithium metal batteries.

Acknowledgements

This work was supported by National Natural Science Foundation of China (21776019, and 21808124), National Key Research and Development Program (2016YFA0202500), Beijing Natural Science Foundation (L182021), and Beijing Key Research and Development Plan (Z181100004518001).

Conflict of interest

The authors declare no conflict of interest.

Keywords: batteries · interfaces · lithium metal anode · quasi-solid-state electrolytes

How to cite: *Angew. Chem. Int. Ed.* **2019**, *58*, 15235–15238
Angew. Chem. **2019**, *131*, 15379–15382

[1] G. N. Lewis, F. G. Keyes, *J. Am. Chem. Soc.* **1913**, *35*, 340–344; X. B. Cheng, R. Zhang, C. Z. Zhao, Q. Zhang, *Chem. Rev.* **2017**, *117*, 10403–10473.
[2] W. Xu, J. Wang, F. Ding, X. Chen, E. Nasybulin, Y. Zhang, J.-G. Zhang, *Energy Environ. Sci.* **2014**, *7*, 513–537.
[3] M. Noel, R. Santhanam, *J. Power Sources* **1998**, *72*, 53–65.
[4] D. C. Lin, Y. Y. Liu, Y. Cui, *Nat. Nanotechnol.* **2017**, *12*, 194–206; C. Yan, H.-R. Li, X. Chen, X.-Q. Zhang, X.-B. Cheng, R. Xu, J.-Q. Huang, Q. Zhang, *J. Am. Chem. Soc.* **2019**, *141*, 9422–9429.
[5] C. Yang, K. Fu, Y. Zhang, E. Hitz, L. Hu, *Adv. Mater.* **2017**, *29*, 1701169.
[6] J. P. Yue, M. Yan, Y. X. Yin, Y. G. Guo, *Adv. Funct. Mater.* **2018**, *28*, 1707533; J. C. Li, C. Ma, M. F. Chi, C. D. Liang, N. J. Dudney, *Adv. Energy Mater.* **2015**, *5*, 1401408; X. Lü, J. W. Howard, A. Chen, J. Zhu, S. Li, G. Wu, P. Dowden, H. Xu, Y. Zhao, Q. Jia, *Adv. Sci.* **2016**, *3*, 1500359; Z. Wei, S. Chen, J. Wang, Z. Wang, Z. Zhang, X. Yao, Y. Deng, X. Xu, *J. Power Sources* **2018**, *394*, 57–66; J. Shim, J. W. Lee, K. Y. Bae, H. J. Kim, W. Y. Yoon, J. C. Lee, *ChemSusChem* **2017**, *10*, 2274–2283; T. C. Liu, L. P. Lin, X. X. Bi, L. L. Tian, K. Yang, J. J. Liu, M. F. Li, Z. H. Chen, J. Lu, K. Amine, K. Xu, F. Pan, *Nat. Nanotechnol.* **2019**, *14*, 50–57; C.-Z. Zhao, P.-Y. Chen, R. Zhang, X. Chen, B.-Q. Li, X.-Q. Zhang, X.-B. Cheng, Q. Zhang, *Sci. Adv.* **2018**, *4*, eaat344; X. Fan, X. Ji, F. Han, J. Yue, J. Chen, L. Chen, T. Deng, J. Jiang, C. Wang, *Sci. Adv.* **2018**, *4*, eaau9245; L. Chen, L. Z. Fan, *Energy Storage Mater.* **2018**, *15*, 37–45; Y. Zhou, X. Wang, H. Zhu, M. Armand, M. Forsyth, G. W. Greene, J. M. Pringle, P. C. Howlett, *Energy Storage Mater.* **2018**, *15*, 407–414; Y. Li, H. Xu, P.-H. Chien, N. Wu, S. Xin, L. Xue, K. Park, Y.-Y. Hu, J. B. Goodenough, *Angew. Chem. Int. Ed.* **2018**, *57*, 8587–8591; *Angew. Chem.* **2018**, *130*, 8723–8727.
[7] S. Wang, H. Xu, W. Li, A. Dolocan, A. Manthiram, *J. Am. Chem. Soc.* **2018**, *140*, 250–257.
[8] Q. Zhao, X. T. Liu, S. Stalin, K. Khan, L. A. Archer, *Nat. Energy* **2019**, *4*, 365–373.
[9] J. Wang, Y. Yamada, K. Sodeyama, E. Watanabe, K. Takada, Y. Tateyama, A. Yamada, *Nat. Energy* **2018**, *3*, 22–29.
[10] K. Karthik, R. Murugan, *J. Solid State Electrochem.* **2018**, *22*, 2989–2998; E. Y. Hu, X. Q. Yu, R. Q. Lin, X. X. Bi, J. Lu, S. M. Bak, K. W. Nam, H. L. L. Xin, C. Jaye, D. A. Fischer, K. Amine, X. Q. Yang, *Nat. Energy* **2018**, *3*, 690–698.
[11] M. Keller, A. Varzi, S. Passerini, *J. Power Sources* **2018**, *392*, 206–225.
[12] L. Fan, S. Wei, S. Li, Q. Li, Y. Lu, *Adv. Energy Mater.* **2018**, *8*, 1702657; W. Luo, C.-F. Lin, O. Zhao, M. Noked, Y. Zhang, G. W. Rubloff, L. Hu, *Adv. Energy Mater.* **2017**, *7*, 1601526; H. Chen, A. Pei, D. Lin, J. Xie, A. Yang, J. Xu, K. Lin, J. Wang, H. Wang, F. Shi, D. Boyle, Y. Cui, *Adv. Energy Mater.* **2019**, *9*, 1900858; L. Suo, W. Xue, M. Gobet, S. G. Greenbaum, C. Wang, Y. Chen, W. Yang, Y. Li, J. Li, *Proc. Natl. Acad. Sci. USA* **2018**, *115*, 1156; X. Fan, L. Chen, X. Ji, T. Deng, S. Hou, J. Chen, J. Zheng, F. Wang, J. Jiang, K. Xu, C. Wang, *Chem* **2018**, *4*, 174–185; Q. Pang, X. Liang, I. R. Kochetkov, P. Hartmann, L. F. Nazar, *Angew. Chem. Int. Ed.* **2018**, *57*, 9795–9798; *Angew. Chem.* **2018**, *130*, 9943–9946; K. Liao, S. Wu, X. Mu, Q. Lu, M. Han, P. He, Z. Shao, H. Zhou, *Adv. Mater.* **2018**, *30*, 1705711; H. Ye, Z.-J. Zheng, H.-R. Yao, S.-C. Liu, T.-T. Zuo, X.-W. Wu, Y.-X. Yin, N.-W. Li, J.-J. Gu, F.-F. Cao, Y.-G. Guo, *Angew. Chem. Int. Ed.* **2019**, *58*, 1094–1099; *Angew. Chem.* **2019**, *131*, 1106–1111.
[13] X. Chen, W. He, L.-X. Ding, S. Wang, H. Wang, *Energy Environ. Sci.* **2019**, *12*, 938–944; T.-T. Zuo, Y. Shi, X.-W. Wu, P.-F. Wang, S.-H. Wang, Y.-X. Yin, W.-P. Wang, Q. Ma, X.-X. Zeng, H. Ye, R. Wen, Y.-G. Guo, *ACS Appl. Mater. Interfaces* **2018**, *10*, 30065–30070; T. Xu, J. Sun, S. Yi, D. Wang, Y. Li, Q. Pei, D. Pan, H. Zhao, Y. Bai, *Solid State Ionics* **2018**, *326*, 110–115; S. Venkatesan, I. P. Liu, J.-C. Lin, M.-H. Tsai, H. Teng, Y.-L. Lee, *J. Mater. Chem. A* **2018**, *6*, 10085–10094; P. Zhang, M. Li, B. Yang, Y. Fang, X. Jiang, G. M. Veith, X.-G. Sun, S. Dai, *Adv. Mater.* **2015**, *27*, 8088–8094; J. A. Lewis, F. J. Q. Cortes, M. G. Boebinger, J. Tippens, T. S. Marchese, N. Kondekar, X. Liu, M. Chi, M. T. McDowell, *ACS Energy Lett.* **2019**, *4*, 591–599; C. Yan, Y. X. Yao, X. Chen, X. B. Cheng, X. Q. Zhang, J. Q. Huang, Q. Zhang, *Angew. Chem. Int. Ed.* **2018**, *57*, 14055–14059; *Angew. Chem.* **2018**, *130*, 14251–14255; X.-Q. Zhang, X. Chen, X.-B. Cheng, B.-Q. Li, X. Shen, C. Yan, J.-Q. Huang, Q. Zhang, *Angew. Chem. Int. Ed.* **2018**, *57*, 5301–5305; *Angew. Chem.* **2018**, *130*, 5399–5403; F. Qiu, X. Li, H. Deng, D. Wang, X. Mu, P. He, H. Zhou, *Adv. Energy Mater.* **2018**, *8*, 1803372; S. Chen, J. Zheng, D. Mei, K. S. Han, M. H. Engelhard, W. Zhao, W. Xu, J. Liu, J.-G. Zhang, *Adv. Mater.* **2018**, *30*, 1706102; H. Zhang, G. G. Eshetu, X. Judez, C. Li, L. M. Rodriguez-Martínez, M. Armand, *Angew. Chem. Int. Ed.* **2018**, *57*, 15002–15027; *Angew. Chem.* **2018**, *130*, 15220–15246.
[14] T. Nakamura, K. Amezawa, J. Kulisch, W. G. Zeier, J. Janek, *ACS Appl. Mater. Interfaces* **2019**, *11*, 19968–19976.
[15] Y. Zhao, L. L. Daemen, *J. Am. Chem. Soc.* **2012**, *134*, 15042–15047.
[16] K. M. Diederichsen, E. J. McShane, B. D. McCloskey, *ACS Energy Lett.* **2017**, *2*, 2563–2575.
[17] J. Betz, J. P. Brinkmann, R. Nolle, C. Lurenbaum, M. Kolek, M. C. Stan, M. Winter, T. Placke, *Adv. Energy Mater.* **2019**, *9*, 1900574.
[18] Z. D. Hood, H. Wang, A. S. Pandian, J. K. Keum, C. Liang, *J. Am. Chem. Soc.* **2016**, *138*, 1768–1771.

Manuscript received: July 16, 2019
Accepted manuscript online: August 5, 2019
Version of record online: August 27, 2019

五项代表性成果/奖励

四、代表性研究论文，锂硫电池界面转化促进机制研究 **(唯一通讯作者，ESI 高被引论文)**。

M. Zhao#, H.-J. Peng#, Z.-W. Zhang, B.-Q. Li, X. Chen, J. Xie, X. Chen, J.-Y. Wei, Q. Zhang, **J.-Q. Huang***. Activating Inert Metallic Compounds for High-Rate Lithium–Sulfur Batteries Through In-Situ Etching of Extrinsic Metal. ***Angew Chem Int Ed*** 2019, 58, 3779.

Batteries

International Edition: DOI: 10.1002/anie.201812062
German Edition: DOI: 10.1002/ange.201812062

Activating Inert Metallic Compounds for High-Rate Lithium–Sulfur Batteries Through In Situ Etching of Extrinsic Metal

*Meng Zhao[+], Hong-Jie Peng[+], Ze-Wen Zhang, Bo-Quan Li, Xiao Chen, Jin Xie, Xiang Chen, Jun-Yu Wei, Qiang Zhang, and Jia-Qi Huang**

Abstract: *Surface reactions constitute the foundation of various energy conversion/storage technologies, such as the lithium–sulfur (Li-S) batteries. To expedite surface reactions for high-rate battery applications demands in-depth understanding of reaction kinetics and rational catalyst design. Now an in situ extrinsic-metal etching strategy is used to activate an inert monometal nitride of hexagonal Ni_3N through iron-incorporated cubic Ni_3FeN. In situ etched Ni_3FeN regulates polysulfide-involving surface reactions at high rates. Electron microscopy was used to unveil the mechanism of in situ catalyst transformation. The Li-S batteries modified with Ni_3FeN exhibited superb rate capability, remarkable cycling stability at a high sulfur loading of 4.8 mg cm^{-2}, and lean-electrolyte operability. This work opens up the exploration of multi-metallic alloys and compounds as kinetic regulators for high-rate Li-S batteries and also elucidates catalytic surface reactions and the role of defect chemistry.*

Surface and interfacial reactions play an essential role in defining various energy-transforming processes, such as solar fuel production and electrochemical energy storage.[1] Today's growing demand for intermittent and discrete energy storage drives the exploration of emerging battery chemistries, such as lithium–sulfur (Li-S) and lithium–air batteries, which often rely on reversible surface electrochemical reactions to afford a high energy density.[2] Expediting these reactions enables the devices with favorable rate performance but often requires reaction mechanism with intrinsically fast kinetics. If the surface reaction mechanism can be in-depth excavated, energy chemistries and related technologies will be advanced expectedly.

[*] M. Zhao,[+] J.-Y. Wei, Prof. J.-Q. Huang
School of Materials Science and Engineering
Beijing Institute of Technology
Beijing 100081 (P. R. China)
E-mail: jqhuang@bit.edu.cn
M. Zhao,[+] J.-Y. Wei, Prof. J.-Q. Huang
Advanced Research Institute of Multidisciplinary Science
Beijing Institute of Technology
Beijing 100081 (P. R. China)
Dr. H.-J. Peng,[+] Z.-W. Zhang, B.-Q. Li, X. Chen, J. Xie, X. Chen, Prof. Q. Zhang
Department of Chemical Engineering, Tsinghua University
Beijing 100084 (P. R. China)
[+] These authors contributed equally to this work.
Supporting information and the ORCID identification number(s) for the author(s) of this article can be found under: https://doi.org/10.1002/anie.201812062.

As a promising substituent to lithium-ion batteries, Li-S batteries afford an attractive specific energy of 2600 Wh kg^{-1} in theory.[3,4] Among various strategies, introducing electrocatalytically active components to the sulfur cathode is recently regarded as an efficient and effective way to accelerate the surface reaction kinetics.[5–8] Rapid surface reactions simultaneously contribute to improving sulfur utilization and mitigating the shuttle effect of soluble polysulfide intermediates, which is often considered as the major origin of capacity fading.[9,10] However, the actual active phases of currently developed electrocatalysis in working conditions have hardly been vigorously validated. Owing to the lack of rational understanding, it is usually by the Edisonian approach to explore new electrocatalysts, rendering the exploration time-consuming and non-precise.[11]

Modern surface science indicates that the catalytic activity often originates from the surface or subsurface defects and vacancies of a solid catalyst.[8,12] Such a general understanding enlightens us to investigate the role of vacancy in electrocatalysis for Li-S batteries and extract core design principles of catalyst design. Thereafter, to explore novel catalysts for polysulfide redox reaction, to enlarge their groups, and to optimize their properties can be realized through composition, phase, and site engineering based on above rationales.

Herein, we demonstrate that the introduction of an extrinsic metal to a monometallic compound, similar to the alloying strategy for metal catalyst design,[13] activates the originally inert phase for kinetic propelling of polysulfide-involving surface reactions at a high rate. Hexagonal nickel nitride (Ni_3N), selected as a proof-of-concept pre-catalyst, was found poorly active for polysulfide mediating, which was transformed into highly active cubic nickel–iron nitride (Ni_3FeN) phase after the incorporation of iron. Both compounds are conductive,[14,15] but the more electropositive iron (compared to nickel) at the corner sites, inclines to be leached out through polysulfide etching, leaving abundant vacant defects around the nickel site to activate it.

Ni_3N and Ni_3FeN nanoparticles were synthesized by ammonolysis (Supporting Information, Figure S1a,b). Both Ni_3N and Ni_3FeN are found as nanoparticles of 10–30 nm in size, supported on wrinkled graphene sheets (denoted as Ni_3N/G and Ni_3FeN/G, respectively). The X-ray diffraction patterns of Ni_3N and Ni_3FeN samples indicate their distinct crystal structures: a hexagonal phase for Ni_3N (JCPDS No. 10-0280, $a=b=4.621$ Å; $c=4.304$ Å),[16] and a cubic phase for Ni_3FeN (JCPDS No. 50-1434, $a=b=c=3.760$ Å; Supporting Information, Figure S1c).[15] The incorporation of iron induces the hexagonal-to-cubic phase transformation. Transmission electron microscopy (TEM) images further indicate

well-indexed lattice fringes with a *d*-spacing of 0.292 nm for the (101) plane of Ni_3N and 0.217 nm for the (111) plane of Ni_3FeN, respectively (Supporting Information, Figure S1d,e).

X-ray photoelectron spectroscopy (XPS) was carried out on Ni_3FeN and Ni_3N before and after reacting with polysulfides to probe their interaction with polysulfides. The incorporation of iron increases the electron density around nickel and nitrogen, inducing obvious red-shifts of Ni^0 $2p_{3/2}$ peaks (from 852.7 eV to 852.0 eV) and N 1s peaks (from 397.8 eV to 396.9 eV) (Figure 1 a and b).[17] The presence of Ni^{2+} can be ascribed to the inevitable oxidation of surface layer (Figure 1 a).[15]

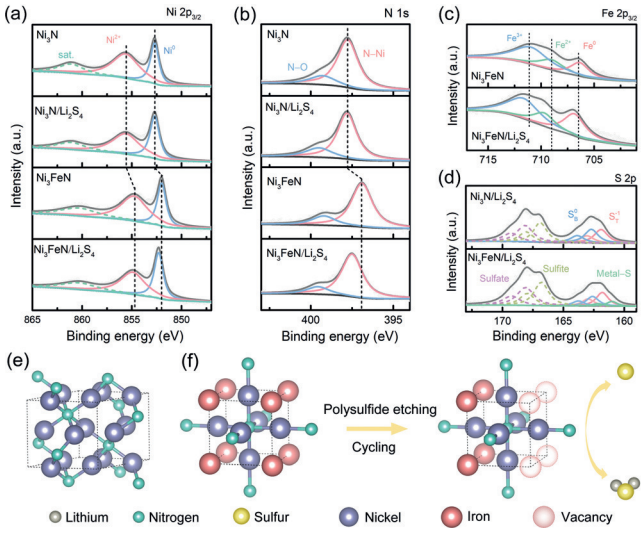

Figure 1. Illustration of the polysulfide-etching-induced activation mechanism. Refined a) Ni 2p, b) N 1s, c) Fe 2p, and d) S 2p XPS spectra of different samples with or without Li_2S_4 addition. e) Atomic structure model of hexagonal Ni_3N. f) Atomic structure model of cubic Ni_3FeN and illustration of the polysulfide etching process toward an active $Ni_3Fe_{1-\delta}N$ phase.

Static adsorption of Li_2S_4 by Ni_3FeN/G and Ni_3N/G aims to simulate the working environment in batteries. A nearly colorless solution after 3.0 h adsorption with Ni_3FeN/G, and a pale yellow solution with Ni_3N/G, imply stronger interaction between polysulfides and Ni_3FeN than Ni_3N (Supporting Information, Figure S2). It can be easily deduced that the more electropositive iron strengthens the adsorption to negatively charged terminal sulfur (S_T) in polysulfides, which is confirmed by the blue-shifts of 0.5 eV for all peaks in the Fe $2p_{3/2}$ spectrum of Ni_3FeN after polysulfide adsorption (denoted as Ni_3FeN/Li_2S_4 and the same for Ni_3N/Li_2S_4), indicating the electron transfer from Fe to S_T (Figure 1 c).

Nevertheless, the effects of extrinsic iron are more than electropositivity. Neither the Ni $2p_{3/2}$ nor N 1s spectrum of Ni_3N/Li_2S_4 exhibits any change compared to that of pristine Ni_3N, indicating no spectroscopically validated chemisorption (Figure 1 a,b). The Ni–N plane of Ni_3N is inert toward polysulfides because of the full coordination of Ni–N in the bulk hexagonal phase, rendering binding sites only available on the surface (Figure 1 e). With iron incorporation, the originally inert Ni–N plane turns into strongly binding toward polysulfides, as indicated by the significant blue-shifts in Ni $2p_{3/2}$ (0.3 eV) and N 1s (0.6 eV) spectra of Ni_3FeN/Li_2S_4 compared to Ni_3FeN (Figure 1 a,b). These blue-shifts suggest the electron transfer from Ni-N to the S_T plane.

The aforementioned difference in interaction paradigm is also validated by the S 2p spectra. Pristine Li_2S_4 exhibited typical $2p_{3/2}/2p_{1/2}$ doublets in the S 2p spectrum at 162.3 and 163.2 eV (referring to $2p_{3/2}$ peaks), attributing to S_T and bridging sulfur (S_B), respectively (Supporting Information, Figure S4).[18] Extra peaks (166.8–169.3 eV) result from oxidation during sample preparation.[19] Ni_3N/Li_2S_4 hardly exhibits a change in the S 2p spectrum (Figure 1 d). In contrast, a new peak at 161.0 eV emerges in the S 2p spectrum of Ni_3FeN/Li_2S_4 and is attributed to the formation of a sulfur–metal (that is, iron and nickel) bond.

Based on above observation, it is speculated that extrinsic iron activates the inert Ni–N plane through a polysulfide-etching-induced vacancy-formation mechanism (Figure 1 f). Iron atoms at the corner sites of cubic structure are leached out via polysulfide etching, as iron is more electropositive than nickel to react with S_T. The removal of iron results in a metastable cubic $Ni_3Fe_{1-\delta}N$ phase (δ refers to the stoichiometric number of vacancies left by iron), which is further stabilized through trapping polysulfides within the vacant defects of $Ni_3Fe_{1-\delta}N$.

Subsequent post-mortem analysis provides further evidence for the above mechanism. As shown in the high-angle annular dark-field scanning transmission electron microscopy (HAADF-STEM) image and corresponding elemental mappings, pristine Ni_3FeN particles exhibit uniform distribution of nickel and iron (Figure 2 a). The linear scan further indicates the overlap of two elements with a small deviation in spatial distribution (Figure 2 b). However, the cycled Ni_3FeN particles are shown with abnormally surface-enriched iron element, implying the phase migration after polysulfide etching (Figure 2 c,d). The migrated species is further identified as a new phase of ferrous sulfide (FeS; Supporting Information, Figure S5), while the cycled Ni_3N sample remains its original phase (Supporting Information, Figure S6). The phase migration is ascribed to the Kirkendall effect and indicates the reaction between polysulfides and Ni_3FeN.

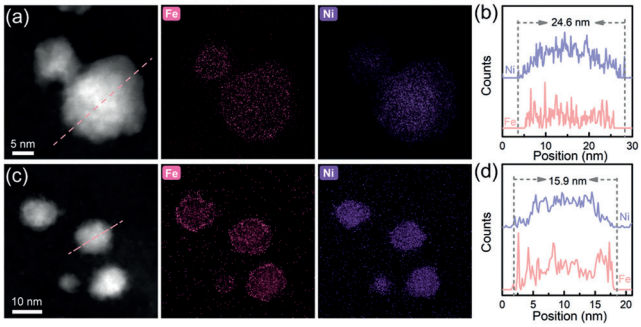

Figure 2. a) HAADF-STEM image of Ni_3FeN-G and the corresponding EDS element distribution. b) Linear elemental distribution of the particle marked in (a). c) HAADF-STEM images of Ni_3FeN-G and the corresponding EDS element distribution after 5 cycles at 0.5 C. d) Linear elemental distribution of the particle marked in (c).

Kinetics of liquid–solid and liquid–liquid reactions were probed to elucidate the effect of extrinsic metal incorporation/removal. Following previous reports,[20] chronoamperometry was employed to probe the liquid–solid nucleation behaviors of lithium sulfide (Li_2S) on various hosts, that is, G, Ni_3N/G, and Ni_3FeN/G (Figure 3a). All three cells reached the highest potentiostatic current after approximately 3500 s, but the integral areas of current peaks varied significantly,

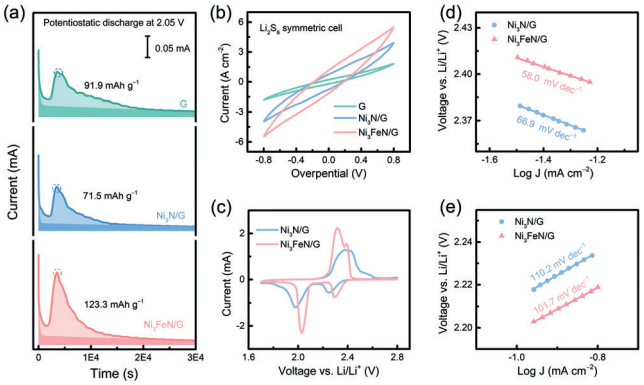

Figure 3. Electrochemical kinetics. a) Chronoamperometry curves of Li_2S_8/tetraglyme solution discharged at 2.05 V on different surfaces. The lighter and darker colored regions indicate the precipitation of Li_2S and the reduction of Li_2S_8/Li_2S_6, respectively. b) CV curves of Li_2S_6 symmetric cells employing different scaffolds as current collectors. c) CV curves of Li-S cells applying a Ni_3N/G- and Ni_3FeN/G-modified separator, respectively. Corresponding Tafel plots for d) the first reduction peak and e) the oxidation peak.

resulting in Li_2S nucleation capacities of 92, 72, and 123 mAh g^{-1} on G, Ni_3N/G, and Ni_3FeN/G, respectively. As the electrode is of equal mass, the sacrifice in surface area for solid precipitation led to small capacity for Ni_3N/G. However, because of the modulation of iron, Ni_3FeN-derived $Ni_3Fe_{1-\delta}N$/G enabled substantially more electrodeposition despite the smaller surface area than G. The morphology characterization of electrodes also reveals that unlike on G and Ni_3N/G, deposited Li_2S layer on Ni_3FeN/G is much thicker, featuring a three-dimensional growth characteristic (Supporting Information, Figure S8).

The liquid–liquid reactions were probed using symmetric cells with a Li_2S_6 electrolyte for cyclic voltammetry (CV) and electrochemical impedance measurements.[21] The redox current responses at a voltage bias of 0.8 V increase in the order of G < Ni_3N/G < Ni_3FeN/G (Figure 3b), while trends in electrochemical impedance has a reverse sequence (Supporting Information, Figure S7). Furthermore, the redox current of FeS/G is comparable to G, further indicating that the active center in Ni_3FeN is mainly the vacancy rather than the iron site on FeS (Supporting Information, Figure S10). These results indicate that the highest charge-transfer rate is between polysulfides and Ni_3FeN/G, which is attributed to stronger ability of vacancies in etched $Ni_3Fe_{1-\delta}N$ to adsorb polysulfides than fully coordinated compounds.

The kinetic-regulating role of $Ni_3Fe_{1-\delta}N$ after iron removal was further demonstrated in actual Li-S batteries. Owing to previous success of modified separators in enhancing Li-S batteries,[18,22] Ni_3FeN/G and Ni_3N/G were filtrated on separators as a catalytic membrane (Supporting Information, Figure S11). The areal sulfur loading is 1.2 mg cm^{-2}, while the loading of Ni_3FeN/G or Ni_3N/G is 0.3 mg cm^{-2}. The CV curves of as-assembled Li-S cells exhibit typical redox peaks: the two cathodic peaks at 2.2–2.3 and 1.9–2.1 V, corresponding to the formation of soluble polysulfides and solid Li_2S, respectively, and two anodic peaks that are partially overlapped, indicating the sequential oxidation of Li_2S and polysulfides (Figure 3c). Compared to non-activated Ni_3N/G, the cell with Ni_3FeN/G possessed less severe polarization for all redox peaks, suggesting better kinetics. Along with the smaller impedance (Supporting Information, Figure S12), the kinetics enhancement is ascribed to the rapid charge transfer between the $Ni_3Fe_{1-\delta}N$ mediator and adsorbed polysulfides.

For quantitative analysis, Tafel plots of the first reduction and oxidation processes are obtained, respectively (Figure 3d,e).[5] The second reduction process was not considered owing to the continuous background current induced by polysulfide interconversion until the onset potential of Li_2S nucleation. For the first reduction, the fitted Tafel slopes of Ni_3FeN/G and Ni_3N/G cells are 58.0 and 66.9 mV dec^{-1}, respectively (Figure 3d); while for the first oxidation, they are 102 and 110 mV dec^{-1}, respectively (Figure 3e). The smaller Tafel slopes for Ni_3FeN/G cell indicate more facile reactions between liquid polysulfides and solid sulfur/Li_2S under the regulation of $Ni_3Fe_{1-\delta}N$ than Ni_3N. Besides, corresponding onset potentials for $Ni_3Fe_{1-\delta}N$-mediated polysulfide redox are about 37 mV positive for sulfur reduction and about 16 mV negative for Li_2S oxidation, also demonstrating the high catalytic activity of $Ni_3Fe_{1-\delta}N$ after iron incorporation/removal.

The rapid polysulfide redox reactions mediated by in situ etched Ni_3FeN provide the Li-S batteries with a superb rate performance (Figure 4a). The cell with a Ni_3FeN/G-modified separator delivered high average capacities of 1309, 1144, 1047, 974, and 905 mAh g^{-1} at 0.1, 0.2, 0.5, 1, and 2 C (1 C = 1672 mAh g^{-1}), which are 9–14% and 11–31% higher than those of Ni_3N/G and FeS/G (Supporting Information, Figure S13). At a high rate of 3 C (6.0 mA cm^{-2}), the Ni_3FeN cell still maintained a high capacity of 822 mAh g^{-1}, while the Ni_3N and FeS cell lost its low discharge plateau. Such a phenomenon is in accordance with the liquid–solid kinetic study, where the Ni_3FeN is shown to improve the Li_2S nucleation rate significantly through strong-binding vacancy sites but the nucleation overpotential on inert Ni_3N at such a high rate is too large to be met by cutoff voltage, leading to early termination of discharge.

The above argument is further validated by galvanostatic discharge–charge profiles (Figure 4b). At a low current density of 0.1 C, the discharge voltages of both cells are comparable despite the higher capacity of the Ni_3FeN cell. However, unlike the smooth transition for the Ni_3FeN cell, the discharge profile of Ni_3N cell exhibits a huge and trailing voltage "dip" at a high rate of 2 C, indicating the sluggish kinetics of Li_2S nucleation/growth on inert Ni_3N and graphene surfaces. Therefore, the sudden capacity decrease for the Ni_3N

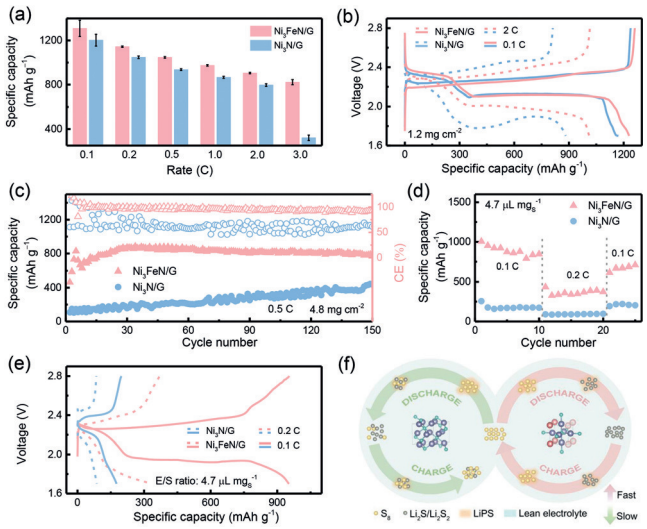

Figure 4. Li-S battery performances. a) Rate performance and b) galvanostatic discharge–charge profiles at different current densities. c) Cycling performance of high-sulfur-loading batteries at 0.5 C. d) Rate performance and e) galvanostatic discharge–charge profiles of lean-electrolyte batteries. Sulfur loading ($mg_{(sulfur)}\,cm^{-2}$): a),b) 1.2; c)–e) 4.8. E/S ratio ($\mu L_{(electrolyte)}\,mg_{(sulfur)}^{-1}$): a),b) 16; c) 14; d),e) 4.7. f) Illustration of Li-S reaction scenarios with different catalysts under lean-electrolyte conditions.

cell at 3 C is expected. Further to Li_2S formation, the incorporation/removal of iron in Ni_3FeN also has a profound influence on Li_2S oxidation. The Ni_3FeN cell generally possessed a barrierless feature at the beginning of charge at both 0.1 and 2 C; while the Ni_3N cell still suffered from an initial charge barrier. Similar to discharge, such a difference is in agreement with Tafel slopes (Figure 3e).

Kinetic regulation enabled by an electrolyte has previously been shown to improve cycling stability of Li-S batteries.[6,10] In this sense, the Ni_3FeN/G cell preserved its 78% of initial capacity after 180 cycles at 1 C, higher than 69% and 54% for the Ni_3N/G cell and the G cell, respectively (Supporting Information, Figures S14 and S15a). Ni_3FeN/G also enabled the cell to be cycled at a 3 C for more than 150 cycles while G and Ni_3N/G could not (Supporting Information, Figure S16a). This can be attributed to the shuttle mitigation by a Ni_3FeN/G separator as the lithium anode with Ni_3FeN/G preserved its morphological compactness mostly when compared to those with G and Ni_3N/G (Supporting Information, Figure S17). Considering the very low mass ratio of Ni_3FeN to sulfur (approximately 1:100 based on thermogravimetric analysis), it is kinetically regulated shuttle "bypassing" rather than chemisorption that accounts for enhanced battery stability.[9]

To further demonstrate the high activity of Ni_3FeN for polysulfide catalysis with an extremely low mass ratio of Ni_3FeN to sulfur (1:400), high-loading cathodes (sulfur loading: 4.8 $mg\,cm^{-2}$) were tested. After an activation process induced by sulfur redistribution,[23] Ni_3FeN/G enabled the sulfur cathode to achieve maximum capacities of 1103 and 900 $mAh\,g^{-1}$ at 0.2 and 0.5 C, along with capacity retention of 75% and 89% after 150 cycles, respectively (Supporting Information, Figure S16b; Figure 4c). In contrast, the control G and Ni_3N/G cells delivered much lower capacities with strong fluctuation of Coulombic efficiencies, suffering from low sulfur utilization and severe shuttle effect at high current densities (Figure 4c; Supporting Information, Figure S15b). Ni_3FeN/G catalyzed Li-S battery has higher rate performance and area capacity, even compared to the recently reported high-sulfur-loading performance (Supporting Information, Table S1).

All of the above electrochemical tests were carried out with substantial excess of electrolyte (electrolyte/sulfur (E/S) ratios of 14–16 $\mu L_{(electrolyte)}\,mg_{(sulfur)}^{-1}$), which is detrimental to the device energy density.[4] Therefore, it is necessary to evaluate the electrocatalyst at a lean-electrolyte condition.[24] At a low E/S ratio of 4.7 $\mu L_{(electrolyte)}\,mg_{(sulfur)}^{-1}$, the Ni_3FeN/G cell delivered high capacities of 1007 and 438 $mAh\,g^{-1}$ at 0.1 and 0.2 C, 3.9 (4.6) and 4.8 (6.2) times than those of Ni_3N/G (FeS/G) (Figure 4d; Supporting Information, Figure S18a). Similar to that at high rates (> 2 C), lean-electrolyte cells exhibit typical charge–discharge curves with Ni_3FeN/G but lose the low discharge plateau with Ni_3N/G and FeS/G (Figure 4e; Supporting Information, Figure S18b). The lean-electrolyte cell evaluation again illustrates the pivotal role of iron incorporation/removal in regulating reactions at harsh working conditions as the vacancy-rich $Ni_3Fe_{1-\delta}N$ phase strengthens the intermediate binding, lowers the reaction barriers, and thus drives more complete sulfur/polysulfide/Li_2S conversion than Ni_3N (Figure 4f).

In summary, we have demonstrated a strategy to activate inert Ni_3N for polysulfide catalysis in Li-S batteries. With the assist from advanced characterization tools such as HAADF-STEM, it was validated that introducing an extrinsic metal (that is, iron) in the Ni_3N triggered the hexagonal-to-cubic phase transformation and this metal can be leached out in situ via polysulfide etching, rendering a highly active vacancy-rich phase to promote the kinetics of polysulfide-involving surface reactions. The Li-S batteries catalyzed by Ni_3FeN exhibited superb rate performance, with a capacity of 822 $mAh\,g^{-1}$ at 3 C, remarkable cycling stability at a high sulfur loading of 4.8 $mg\,cm^{-2}$ (89% capacity retention after 150 cycles), and lean-electrolyte operability. This work not only describes an extrinsic-metal activation mechanism for non-active monometal compounds but also elucidates the important role of in situ phase evolution and vacancy formation in regulating catalytic reactions. Therefore, this work opens up the exploration of multimetallic alloys and compounds for Li-S battery kinetics regulation and also enlighten understanding of surface reactions and catalyst design.

Acknowledgements

This work was supported by National Key Research and Development Program (2016YFA0202500 and 2016YFA0200102), National Natural Science Foundation of China (21776019 and 21676160), Beijing Key Research and Development Plan (Z181100004518001).

Conflict of interest

The authors declare no conflict of interest.

Keywords: electrocatalysis · lithium–sulfur batteries · metal nitrides · polysulfide redox reaction · separators

How to cite: *Angew. Chem. Int. Ed.* **2019**, *58*, 3779–3783
Angew. Chem. **2019**, *131*, 3819–3823

[1] J. H. Montoya, L. C. Seitz, P. Chakthranont, A. Vojvodic, T. F. Jaramillo, J. K. Norskov, *Nat. Mater.* **2017**, *16*, 70–81; N. S. Choi, Z. H. Chen, S. A. Freunberger, X. L. Ji, Y. K. Sun, K. Amine, G. Yushin, L. F. Nazar, J. Cho, P. G. Bruce, *Angew. Chem. Int. Ed.* **2012**, *51*, 9994–10024; *Angew. Chem.* **2012**, *124*, 10134–10166.

[2] P. G. Bruce, S. A. Freunberger, L. J. Hardwick, J. M. Tarascon, *Nat. Mater.* **2012**, *11*, 19–29.

[3] Y. X. Yin, S. Xin, Y. G. Guo, L. J. Wan, *Angew. Chem. Int. Ed.* **2013**, *52*, 13186–13200; *Angew. Chem.* **2013**, *125*, 13426–13441; Q. Pang, X. Liang, C. Y. Kwok, L. F. Nazar, *Nat. Energy* **2016**, *1*, 16132; H. J. Peng, J. Q. Huang, X. B. Cheng, Q. Zhang, *Adv. Energy Mater.* **2017**, *7*, 1700260; S. M. Xu, D. W. McOwen, L. Zhang, G. T. Hitz, C. W. Wang, Z. H. Ma, C. J. Chen, W. Luo, J. Q. Dai, Y. D. Kuang, E. M. Hitz, K. Fu, Y. H. Gong, E. D. Wachsman, L. B. Hu, *Energy Storage Mater.* **2018**, https://doi.org/10.1016/j.ensm.2018.1008.1009.

[4] R. P. Fang, S. Y. Zhao, Z. H. Sun, W. Wang, H. M. Cheng, F. Li, *Adv. Mater.* **2017**, *29*, 1606823; S. H. Chung, C. H. Chang, A. Manthiram, *Adv. Funct. Mater.* **2018**, *28*, 1801188.

[5] H. Al Salem, G. Babu, C. V. Rao, L. M. R. Arava, *J. Am. Chem. Soc.* **2015**, *137*, 11542–11545.

[6] Z. Yuan, H. J. Peng, T. Z. Hou, J. Q. Huang, C. M. Chen, D. W. Wang, X. B. Cheng, F. Wei, Q. Zhang, *Nano Lett.* **2016**, *16*, 519–527.

[7] Z. H. Sun, J. Q. Zhang, L. C. Yin, G. J. Hu, R. P. Fang, H. M. Cheng, F. Li, *Nat. Commun.* **2017**, *8*, 14627; G. M. Zhou, H. Z. Tian, Y. Jin, X. Y. Tao, B. F. Liu, R. F. Zhang, Z. W. Seh, D. Zhuo, Y. Y. Liu, J. Sun, J. Zhao, C. X. Zu, D. S. Wu, Q. F. Zhang, Y. Cui, *Proc. Natl. Acad. Sci. USA* **2017**, *114*, 840–845; T. G. Jeong, D. S. Choi, H. Song, J. Choi, S. A. Park, S. H. Oh, H. Kim, Y. Jung, Y. T. Kim, *ACS Energy Lett.* **2017**, *2*, 327–333; H. D. Yuan, X. L. Chen, G. M. Zhou, W. K. Zhang, J. M. Luo, H. Huang, Y. P. Gan, C. Liang, Y. Xia, J. Zhang, J. G. Wang, X. Y. Tao, *ACS Energy Lett.* **2017**, *2*, 1711–1719; Y. R. Zhong, L. C. Yin, P. He, W. Liu, Z. S. Wu, H. L. Wang, *J. Am. Chem. Soc.* **2018**, *140*, 1455–1459; J. C. Ye, J. J. Chen, R. M. Yuan, D. R. Deng, M. S. Zheng, L. Cronin, Q. F. Dong, *J. Am. Chem. Soc.* **2018**, *140*, 3134–3138; J. T. Zhang, Z. Li, Y. Chen, S. Y. Gao, X. W. Lou, *Angew. Chem. Int. Ed.* **2018**, *57*, 10944–10948; *Angew. Chem.* **2018**, *130*, 11110–11114; L. Luo, S. H. Chung, H. Y. Asl, A. Manthiram, *Adv. Mater.* **2018**, *30*, 1804149; C. Luo, H. L. Zhu, W. Luo, F. Shen, X. L. Fan, J. Q. Dai, Y. J. Liang, C. S. Wang, L. B. Hu, *ACS Appl. Mater. Interfaces* **2017**, *9*, 14801–14807; D. R. Deng, F. Xue, Y. J. Jia, J. C. Ye, C. D. Bai, M. S. Zheng, Q. F. Dong, *ACS Nano* **2017**, *11*, 6031–6039; Y. Zhong, D. L. Chao, S. J. Deng, J. Y. Zhan, R. Y. Fang, Y. Xia, Y. D. Wang, X. L. Wang, X. H. Xia, J. P. Tu, *Adv. Funct. Mater.* **2018**, *28*, 1706391; L. L. Zhang, X. Chen, F. Wan, Z. Q. Niu, Y. J. Wang, Q. Zhang, J. Chen, *ACS Nano* **2018**, *12*, 9578–9586; T. H. Zhou, W. Lv, J. Li, G. M. Zhou, Y. Zhao, S. X. Fan, B. L. Liu, B. H. Li, F. Y. Kang, Q. H. Yang, *Energy Environ. Sci.* **2017**, *10*, 1694–1703; S. Yun, S. H. Park, J. S. Yeon, J. Park, M. Jana, J. Suk, H. S. Park, *Adv. Funct. Mater.* **2018**, *28*, 1707593.

[8] H. B. Lin, L. Q. Yang, X. Jiang, G. C. Li, T. R. Zhang, Q. F. Yao, G. W. Zheng, J. Y. Lee, *Energy Environ. Sci.* **2017**, *10*, 1476–1486.

[9] H. J. Peng, Q. Zhang, *Angew. Chem. Int. Ed.* **2015**, *54*, 11018–11020; *Angew. Chem.* **2015**, *127*, 11170–11172.

[10] Z. W. Zhang, H. J. Peng, M. Zhao, J. Q. Huang, *Adv. Funct. Mater.* **2018**, *28*, 1707536.

[11] Z. W. Seh, J. Kibsgaard, C. F. Dickens, I. B. Chorkendorff, J. K. Norskov, T. F. Jaramillo, *Science* **2017**, *355*, eaad4998.

[12] D. F. Yan, Y. X. Li, J. Huo, R. Chen, L. M. Dai, S. Y. Wang, *Adv. Mater.* **2017**, *29*, 1606459; H. Li, C. Tsai, A. L. Koh, L. L. Cai, A. W. Contryman, A. H. Fragapane, J. H. Zhao, H. S. Han, H. C. Manoharan, F. Abild-Pedersen, J. K. Norskov, X. L. Zheng, *Nat. Mater.* **2016**, *15*, 48–54.

[13] J. Greeley, T. F. Jaramillo, J. Bonde, I. B. Chorkendorff, J. K. Norskov, *Nat. Mater.* **2006**, *5*, 909–913.

[14] K. Xu, P. Z. Chen, X. L. Li, Y. Tong, H. Ding, X. J. Wu, W. S. Chu, Z. M. Peng, C. Z. Wu, Y. Xie, *J. Am. Chem. Soc.* **2015**, *137*, 4119–4125.

[15] X. D. Jia, Y. F. Zhao, G. B. Chen, L. Shang, R. Shi, X. F. Kang, G. I. N. Waterhouse, L. Z. Wu, C. H. Tung, T. R. Zhang, *Adv. Energy Mater.* **2016**, *6*, 1502585.

[16] D. Q. Gao, J. Y. Zhang, T. T. Wang, W. Xiao, K. Tao, D. S. Xue, J. Ding, *J. Mater. Chem. A* **2016**, *4*, 17363–17369.

[17] B. R. Xia, T. T. Wang, X. Chi, X. J. Yu, P. T. Liu, J. Y. Zhang, S. B. Xi, Y. H. Du, D. Q. Gao, *Appl. Phys. Lett.* **2017**, *111*, 232402.

[18] H. J. Peng, Z. W. Zhang, J. Q. Huang, G. Zhang, J. Xie, W. T. Xu, J. L. Shi, X. Chen, X. B. Cheng, Q. Zhang, *Adv. Mater.* **2016**, *28*, 9551–9558.

[19] X. Liang, C. Y. Kwok, F. Lodi-Marzano, Q. Pang, M. Cuisinier, H. Huang, C. J. Hart, D. Houtarde, K. Kaup, H. Sommer, T. Brezesinski, J. Janek, L. F. Nazar, *Adv. Energy Mater.* **2016**, *6*, 1501636.

[20] F. Y. Fan, W. C. Carter, Y. M. Chiang, *Adv. Mater.* **2015**, *27*, 5203–5209.

[21] H. J. Peng, G. Zhang, X. Chen, Z. W. Zhang, W. T. Xu, J. Q. Huang, Q. Zhang, *Angew. Chem. Int. Ed.* **2016**, *55*, 12990–12995; *Angew. Chem.* **2016**, *128*, 13184–13189.

[22] S. H. Chung, A. Manthiram, *Adv. Funct. Mater.* **2014**, *24*, 5299–5306; H. J. Peng, D. W. Wang, J. Q. Huang, X. B. Cheng, Z. Yuan, F. Wei, Q. Zhang, *Adv. Sci.* **2016**, *3*, 1500268.

[23] X. Q. Yu, H. L. Pan, Y. N. Zhou, P. Northrup, J. Xiao, S. M. Bak, M. Z. Liu, K. W. Nam, D. Y. Qu, J. Liu, T. P. Wu, X. Q. Yang, *Adv. Energy Mater.* **2015**, *5*, 1500072; H. J. Peng, J. Q. Huang, X. Y. Liu, X. B. Cheng, W. T. Xu, C. Z. Zhao, F. Wei, Q. Zhang, *J. Am. Chem. Soc.* **2017**, *139*, 8458–8466.

[24] Y. X. Yang, Y. R. Zhong, Q. W. Shi, Z. H. Wang, K. N. Sun, H. L. Wang, *Angew. Chem. Int. Ed.* **2018**, *57*, 15549–15552; *Angew. Chem.* **2018**, *130*, 15775–15778.

Manuscript received: October 21, 2018
Revised manuscript received: November 28, 2018
Accepted manuscript online: December 12, 2018
Version of record online: January 16, 2019

五项代表性成果/奖励

五、代表性研究论文，金属锂内亥姆霍兹层影响初始固液界面形成和输运特性研究 **(唯一通讯作者)**

C. Yan, H.-R. Li, X. Chen, X.-Q. Zhang, X.-B. Cheng, R. Xu, **J.-Q. Huang***, Q. Zhang. Regulating the Inner Helmholtz Plane for Stable Solid Electrolyte Interphase on Lithium Metal Anodes. ***J Am Chem Soc*** 2019, 141, 9422.

JACS
JOURNAL OF THE AMERICAN CHEMICAL SOCIETY
Article
Cite This: J. Am. Chem. Soc. 2019, 141, 9422−9429
pubs.acs.org/JACS

Regulating the Inner Helmholtz Plane for Stable Solid Electrolyte Interphase on Lithium Metal Anodes

Chong Yan,[†,‡] Hao-Ran Li,[§] Xiang Chen,[§] Xue-Qiang Zhang,[§] Xin-Bing Cheng,[§] Rui Xu,[†,‡] Jia-Qi Huang,[*,†] and Qiang Zhang[§]

[‡]School of Materials Science & Engineering, Beijing Institute of Technology, Beijing 100081, China
[†]Advanced Research Institute of Multidisciplinary Science, Beijing Institute of Technology, Beijing 100081, China
[§]Beijing Key Laboratory of Green Chemical Reaction Engineering and Technology, Department of Chemical Engineering, Tsinghua University, Beijing 100084, China

Supporting Information

ABSTRACT: The stability of a battery is strongly dependent on the feature of solid electrolyte interphase (SEI). The electrical double layer forms prior to the formation of SEI at the interface between the Li metal anode and the electrolyte. The fundamental understanding on the regulation of the SEI structure and stability on Li surface through the structure of the electrical double layer is highly necessary for safe batteries. Herein, the interfacial chemistry of the SEI is correlated with the initial Li surface adsorption electrical double layer at the nanoscale through theoretical and experimental analysis. Under the premise of the constant solvation sheath structure of Li^+ in bulk electrolyte, a trace amount of lithium nitrate ($LiNO_3$) and copper fluoride (CuF_2) were employed in electrolytes to build robust electric double layer structures on a Li metal surface. The distinct results were achieved with the initial competitive adsorption of bis(fluorosulfonyl)imide ion (FSI^-), fluoride ion (F^-), and nitrate ion (NO_3^-) in the inner Helmholtz plane. As a result, Cu−NO_3^- complexes are preferentially adsorbed and reduced to form the SEI. The modified Li metal electrode can achieve an average Coulombic efficiency of 99.5% over 500 cycles, enabling a long lifespan and high capacity retention of practical rechargeable batteries. The as-proposed mechanism bridges the gap between Li^+ solvation and the adsorption about the electrode interface formation in a working battery.

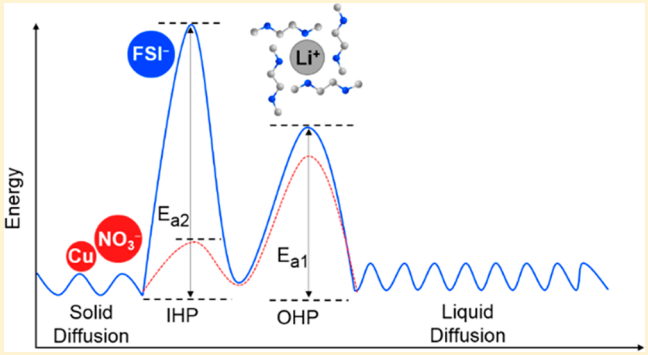

INTRODUCTION

The state-of-the-art lithium ion batteries (LIBs) have reached a bottleneck with the capacity limitation of graphite anode in meeting the demanding energy density for high-end electronics and electric vehicles.[1] Alternatively, Li metal anodes are reviving and ushering in the emerging opportunities due to their high theoretical specific capacity (3860 mAh g^{-1}) and low electrode potential (−3.04 V vs the standard hydrogen electrode).[2] Therefore, Li−sulfur, Li−oxygen, and solid state batteries, which rely on the use of Li metal anodes, exhibit huge potentials in portable electronics, unmanned aerial vehicles, and electric vehicles.[3] Actually, the fundamental research on Li metal batteries (LMBs) was carried out before that of LIBs. However, the highly reactive Li and its extremely air sensitive interfaces seriously have hindered further progress.[4]

Nowadays, advanced characterization techniques and novel modeling facilitate us to get closer insight into the actual essence.[5,6] Recent investigations concluded that Coulombic efficiency (CE) as well as dendrite inhibition were strongly relying on the stability of the electrode interface.[7] Regulating the solvation sheath structure of Li^+ in bulk electrolytes affords a facile and efficient method in controllable formation of the solid electrolyte interphase (SEI).[8−11] There are many chemical species around the primary solvation sheath of Li^+ that play a more crucial role than the secondary sheath as the primary sheath is preferentially reduced at the electrode surface. Therefore, the relationship between Li^+ solvation in bulk electrolyte and the structures/properties of the SEI is strongly requested.[12−15]

The inner structure of the electric double layer on the Li surface is defined as the inner Helmholtz plane (IHP). The IHP is strongly associated with the following formation of the SEI. Note that the thickness of the IHP is at the nanoscale, indicating solvated Li^+ is not allowed in the IHP.[16−18] The research focusing on the IHP in aqueous Li-ion batteries has been studied by Wang and co-workers.[19,20] The surplus anions will preferentially decompose to form a stable SEI in aqueous electrolyte; thus, the water is almost excluded from direct contact with the graphite surface. However, there is a

Received: May 10, 2019
Published: May 22, 2019

DOI: 10.1021/jacs.9b05029
J. Am. Chem. Soc. 2019, 141, 9422−9429

fundamental understanding gap between the adsorption in the IHP of the nonaqueous Li surface and solvated Li^+ in configuring the SEI layer.

In this contribution, we investigated different adsorption species on the Li metal anode that consists of the IHP through theoretical and experimental analysis under the premise of the constant solvation sheath structure of Li^+ in bulk electrolyte. By correlating the initial competitive adsorption of the IHP with the formation of the SEI layer, we completed the whole scenario of premier adsorption in the IHP and the solvation sheath structure of Li^+ in bulk electrolytes, which contribute to the fresh insights into the interfacial chemistry of SEI formation on the Li metal anode.

EXPERIMENTAL SECTION

Materials. Both the routine Li metal foil (500 μm) and ultrathin Li metal foil (50 μm) were commercially available from China Energy Lithium Co., Ltd. The solvents of 1,2-dimethoxyethane (DME) were purchased from Beijing Institute of Chemical Reagents. Lithium bis(fluorosulfonyl)imide (LiFSI), lithium nitrate ($LiNO_3$), and copper fluoride (CuF_2) were purchased from Alfa Aesar. All lithium salts were analytically pure. Lithium iron phosphate ($LiFePO_4$, LFP) cathodes (LFP coated on Al foil) were purchased from Shenzhen Kejing Star Technology Co., Ltd., containing 80 wt % active materials, 10 wt % super P, and 10 wt % polyvinylidene fluoride (PVDF) binder. The areal loadings of LFP cathodes were about 13.7 mg cm^{-2} with a capacity of 2.0 mAh cm^{-2}. All of the electrodes were dried under a vacuum at 100 °C for 6 h before use.

Structure Characterizations. The ^{13}C nuclear magnetic resonance (NMR) experiments were performed on a JNM-ECA600 NMR spectrometer. The deuterated chloroform ($CDCl_3$) was employed as the dispersion to lock field of electrolyte, and the NMR spectra of $CDCl_3$ in nonaqueous electrolytes are shown in Figure S1. The total mass of the electrolyte in NMR experiments is ca. 80 mg. The deposition morphologies of the Li on copper substrate were characterized by SEM (JSM 7401F, JEOL Ltd., Japan) operated at 10.0 kV. The structure and energy dispersion spectrum (EDS) of SEI covered on the lithium anode after cycling were characterized by STEM (FEI Titan Cube Themis G2 300). The first cycled anode was washed with DME to remove residual lithium salt and then put into DME solution for 2 h of ultrasonic cleanout. In order to minimize radiation damage of electrons to the samples, the operating voltage is 60 kV. The crystal phase of lithium foil was analyzed by X-ray diffraction (XRD, D_8 Advance, Bruker Inc. Germany). Al K1α radiation (pass energy 55.0 eV) at a pressure lower than 10^{-7} Torr was applied to acquire XPS spectra on PHI Quantera SXM (ULVAC-PHI, Inc. Japan). The analyzed area of lithium foil was about 5 mm × 5 mm. The binding energies of the involved elements were corrected by C 1s at 284.8 eV. Both the copper substrates and lithium electrodes used in characterizations were washed by DME solvents and then dried in the glovebox until the solvent was volatilized totally. During the transferring process before any characterization, all samples were protected in Ar-filled containers to avoid direct contact with air.

Electrochemical Measurements. Different concentrations of LiFSI salt were dissolved in DME to prepare the LiFSI/DME electrolyte, and then, 20 mmol L^{-1} CuF_2 and 20 mmol L^{-1} $LiNO_3$ were added into LiFSI/DME to prepare NF-LiFSI/DME electrolyte. The 20 mmol L^{-1} $LiNO_3$ or $Cu(NO_3)_2$ was individually added into 2.3 mol L^{-1} (M) LiFSI/DME to prepare 2.3 M LiFSI/DME−$LiNO_3$ or 2.3 M LiFSI/DME−$Cu(NO_3)_2$ electrolyte. All of the solution was kept for 24 h until it completely dissolved. Cu foil was punched into disks with a diameter of 19.0 mm as the working electrodes, and the Li metal foils had a diameter of 17.0 mm. In linear sweep voltammetry (LSV) measurement, Li metal was both the reference electrode and the counter electrode, while the Cu foil was taken as the working electrode. In the alternating current voltammetry tests, the frequency is 6 Hz and the amplitude (A) is 5 mV, with a potential range extended from 2.0 to 1.5 V versus Li^+/Li. The selective region of phase angles was 0 and 90°. The capacitance is calculated with the method mentioned above.[21] The EIS measurements of coin cells under different temperatures were conducted in a CT4005 high-low temperature chamber (Chongqing SD Experiment Instrument Co., Ltd.), and the frequency ranged from 10^5 to 10^{-1} Hz under a voltage amplitude of 10 mV. All of the electrochemical measurements were conducted on a Solartron 1470E electrochemical workstation (Solartron Analytical, U.K.). The Coulombic efficiency measurement was employed by Li|Cu cells, and the stability test of the Li electrode was measured by Li|Li symmetrical cells. The current density is 1.0 and 3.0 mA cm^{-2} with capacities of 1.0 and 3.0 mAh cm^{-2}, respectively. The Li|LFP CR2032 coin cells with a capacity of 2.0 mAh cm^{-2} were cycled at 1.0 C (≈172 mA g^{-1} based on LFP cathode materials) within a voltage range of 2.8−4.0 V versus Li^+/Li. These battery cycling tests were all conducted using a LAND multichannel battery cycler (Wuhan LAND Electronics Co., Ltd.). The tests of cells were taken at a temperature of 25 °C. Except for some special statements, 2032 coin-type cells were assembled in an Ar-filled glovebox with O_2 and H_2O content below 0.1 ppm. The electrolyte volume was 20 μL in total in both LFP|Li and Li|Li coin cells. The pouch cell was fabricated through a layer-by-layer strategy with five pieces of cathode and four pieces of anode as a group. The area of each electrode was 15 cm^2 (50 mm × 30 mm). A high areal LFP loading of 13.7 mg cm^{-2} and a total capacity of 250 mAh were achieved in a pouch cell, and the electrolyte volume was 1000 μL in total in a LFP|Li pouch cell. The type of separator is Celgard 2400, whose thickness is 25 μm. The copper foil was immersed in 1.0 M diluted hydrochloric acid (HCl) for 15 min and followed by rinsing in ethanol before testing in a cell. The lithium foils that were used in our experiments were polished with tetrahydrofuran (THF) solvents. After that, the polished lithium foils were washed with nonpolar solvent (n-hexane) and dried naturally.

Simulation Details. The first-principles calculations were conducted in the Vienna ab initio Simulation Package (VASP) program with projector augmented wave (PAW) for the electronic core states.[22−24] The generalized gradient approximation (GGA) with the parametrization of Perdew−Burke−Ernzerhof (PBE)[25] was used to treat the exchange correlation energy of interactive electrons. The plane wave cutoff energy is set to be 520 eV. Lattice parameters and atomic coordinates were all fully relaxed to an energy convergence of 10^{-5} eV. A vacuum of 20 Å was added into the z direction to avoid the periodic interactions between slabs. The five-layer Li(100) slab with dimensions of 10.3 Å × 10.3 Å × 26.9 Å was used, and the bottom two layers were fixed. When considering the interaction between the slab and the adsorbed species, two basic ion pair models were considered: Slab−Li^+−A^- and Slab−A^-−Li^+, where A^- represents the anions from Li salts (FSI^-, F^-, and NO_3^-). In the Slab−Li^+−A^- model, the Li^+ was allowed to relax on the Li slab and the A^- was fixed in the vacuum, while, in the Slab−A^-−Li^+ model, the A^- was allowed to relax on the Li slab and the Li^+ was fixed in the vacuum.

The binding energy (E_b) between LiFSI/LiF/$LiNO_3$ and the Li metal surface was defined as follows

$$E_b = E_{total} - E_{ion\ pair} - E_{slab}$$

where E_{total}, $E_{ion\ pair}$, and E_{slab} are the total energy of the adsorption model, the energy of an ion pair of LiFSI, LiF, or $LiNO_3$, and the energy of the Li slab, respectively.

RESULTS AND DISCUSSION

Electrochemical Performance. By adding a trace amount (20 mmol L^{-1} each) of $LiNO_3$ and CuF_2 into 2.3 M lithium bis(fluorosulfonyl)imide (LiFSI)/1,2-dimethoxyethane (DME) electrolyte (the 2.3 M electrolyte is denoted by LiFSI/DME, while the modified electrolyte is denoted by NF-LiFSI/DME), the solvation structure of Li^+ in bulk solution is kept constant (Figure S1). Nevertheless, the electrochemical profiles of the $LiFePO_4$ (LFP)|Li batteries at a cycle rate of 1.0 C and the Cu/Li batteries at 1.0 mA cm^{-2} differ significantly in these two electrolytes.

DOI: 10.1021/jacs.9b05029
J. Am. Chem. Soc. 2019, 141, 9422−9429

The LFP|Li battery with NF-LiFSI/DME electrolyte exhibits at least 11 times longer lifespan than the cell with LiFSI/DME electrolyte (Figure 1a). The applications of NF-LiFSI/DME

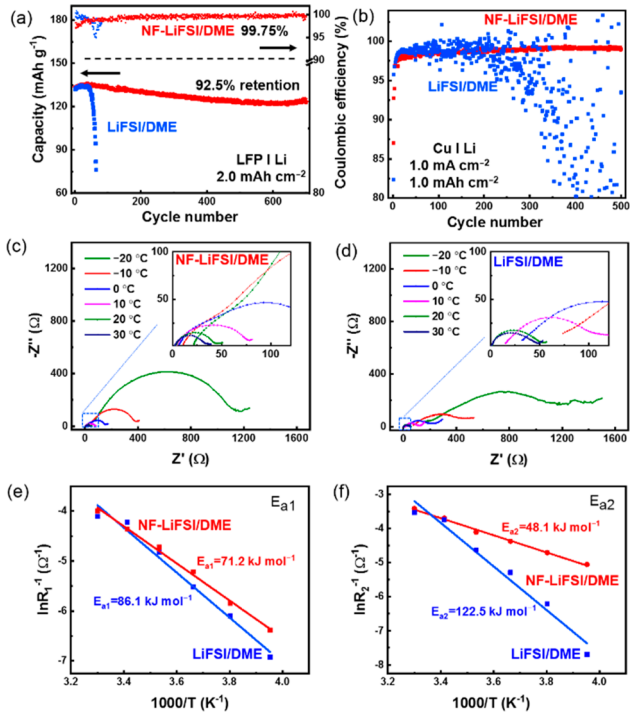

Figure 1. Electrochemical performance of the Li anode based coin cell in LiFSI/DME and NF-LiFSI/DME electrolyte. (a) The cycle life and CE of Li|LiFePO$_4$ coin cells at 1.0 C. (b) Cycling performance of Li|Cu coin cells at 1.0 mA cm^{-2} with 1.0 mAh cm^{-2} capacity. (c and d) Nyquist plots of the Li|Li cells at different temperatures. (e and f) Arrhenius behavior and comparison of activation energies between the R_1 and R_2 derived in Nyquist plots of Li|Li symmetrical cells.

electrolyte obviously postpone cell failure and reduce the hysteretic voltage (Figure S2). Meanwhile, the utilization of Li during cycling is remarkably promoted (average CE of 99.5% even after 500 cycles) (Figure 1b), indicating the integrated interphase formed on the Li anode. A very harsh condition with a large current density of 3.0 mAh cm^{-2} and an ultrathin Li foil (decreased from 200 to 50 μm in thickness) was configured in Cu|Li and Li|Li cells, respectively, to further probe the stability of the SEI. The average CE in NF-LiFSI/DME is 99.6% (Figure S3a), and the Li interphase constantly remains unscathed even after 1000 h of stripping/plating (Figure S3b). In contrast, the CE in the cell with LiFSI/DME is highly fluctuant. The symmetric batteries with ultrathin Li exhibit a short circuit after 790 h (Figure S3). The poor performances were ascribed to the continuous damage/reconstruction of the SEI and the continuous growth of Li dendrites.

In addition, the electrochemical performance of LFP|Li cells in other liquid electrolytes was also tested. In contrast to the severe decomposition of electrolyte in 1.0 M LiFSI/DME, whose lifespan is only seven cycles (Figure S4), the addition of trace amounts of CuF_2 and $LiNO_3$ in 1.0 M LiFSI/DME can significantly prolong the lifespan up to 6 times (Figure S5a). This confirms the CuF_2 and $LiNO_3$ induced SEI at the initial cycle can inhibit the decomposition of electrolyte. However, the poor solvation environment of electrolyte damages the SEI formed on lithium metal during repeated cycling; the evolution behavior of the SEI layer in dilute solution (1.0 M) was abandoned in this contribution. The electrochemical performance of the LFP|Li cell in 2.3 M LiFSI/DME with the sole $LiNO_3$ or $Cu(NO_3)_2$ additive was also evaluated, the cycle lifespan of which was 160 and 301 (Figure S5b and c), respectively. Therefore, by summarizing the data of different electrolyte systems (Figure S5d), we conclude that nitrate ion (NO_3^-), fluoride ion (F^-), and copper ion (Cu^{2+}) all functioned positively in prolonging the battery life. The deep reason behind the different ions in electrolytes is the distinct composition and structure of the SEI. In the following discussion, we mainly focus on the dynamical behavior for Li^+ transport through the SEI layer and the formation of the SEI layer in NF-LiFSI/DME and LiFSI/DME electrolytes.

Ogumi and co-workers described that the transport of Li^+ through the SEI and the so-called charge-transfer process exhibited a close dependence on temperature, which had been verified by electrochemical impedance spectroscopy (EIS) measurement.[26] Herein, the equivalent circuit models were established according to the as-obtained EIS profiles at different frequencies (Figure S6). The activation energies (E_a) representing the journey of Li^+ were obtained through fitting the separated semicircles (R_1, R_2) in Li|Li symmetrical batteries (Figure 1c–f). Both E_{a1} and E_{a2} are in line with the law of Arrhenius. E_{a1}, representing the transport process of Li^+ in SEI film, is 71.2 kJ mol^{-1} in NF-LiFSI/DME, slightly smaller than that in LiFSI/DME (86.1 kJ mol^{-1}). NF-LiFSI/DME electrolyte renders a stable SEI layer with a low energy barrier for Li^+ transportation. E_{a2}, representing the desolvation energy of Li^+, is related to the solvation sheath structure as well as the SEI layer, which is also denoted as the charge transfer activation energy. This has been widely accepted as the dominant barrier in the electrochemical process.[27] However, it exhibits a distinct decrease in NF-LiFSI/DME (Figure 1f). Even when the solvation sheath structure of Li^+ remains constant in bulk electrolyte, disparity of E_{a2} is nonetheless observed. It is inferred that the initial electric double layers on the Li surface, including the IHP and the outer Helmholtz plane (OHP), have a significant effect on the formation of the SEI layer.

Competition of Adsorption. The IHP is defined as the locus of the electrical center of specially adsorbed ions. The components of the IHP are strongly related to the properties of electrodes and electrolytes, although the specially adsorbed ions are anions in most cases irrespective of the charge nature of the electrode.[28] Herein, first-principles calculations were conducted to confirm the specially adsorbed ions on lithium metal anodes and thus identify the IHP. Two basic ion pair models were considered: Slab−Li^+−A^- and Slab−A^-−Li^+, where A^- represents the anions from Li salts (FSI^-, NO_3^-, and F^-). In the Slab−Li^+−A^- model, the Li^+ was allowed to relax on the Li slab and the A^- was fixed in the vacuum, while, in the Slab−A^-−Li^+ model, the A^- was allowed to relax on the Li slab and the Li^+ was fixed in the vacuum. The geometrical structures and binding energies of these interactions are summarized in Figure 2 and Figure S7. Generally, the Li slab affords a much larger binding energy toward anions (−4.44 to −6.35 eV) than Li^+ (−1.96 to −1.50 eV), which is consistent with previous reports that anions dominate in the IHP.[29−31] The large binding energies of anions are induced by the as-formed strong Li−O/N/F interactions as well as a significant charge transfer. The Li−O/Li−N bond lengths are 2.024/1.804 and 2.201/2.341 Å in the FSI^- and NO_3^- models, respectively, similar to that in Li_2O (2.017 Å) and Li_3N (2.108 Å) crystals (Figure 2f). The Li−F bond length is

DOI: 10.1021/jacs.9b05029
J. Am. Chem. Soc. 2019, 141, 9422−9429

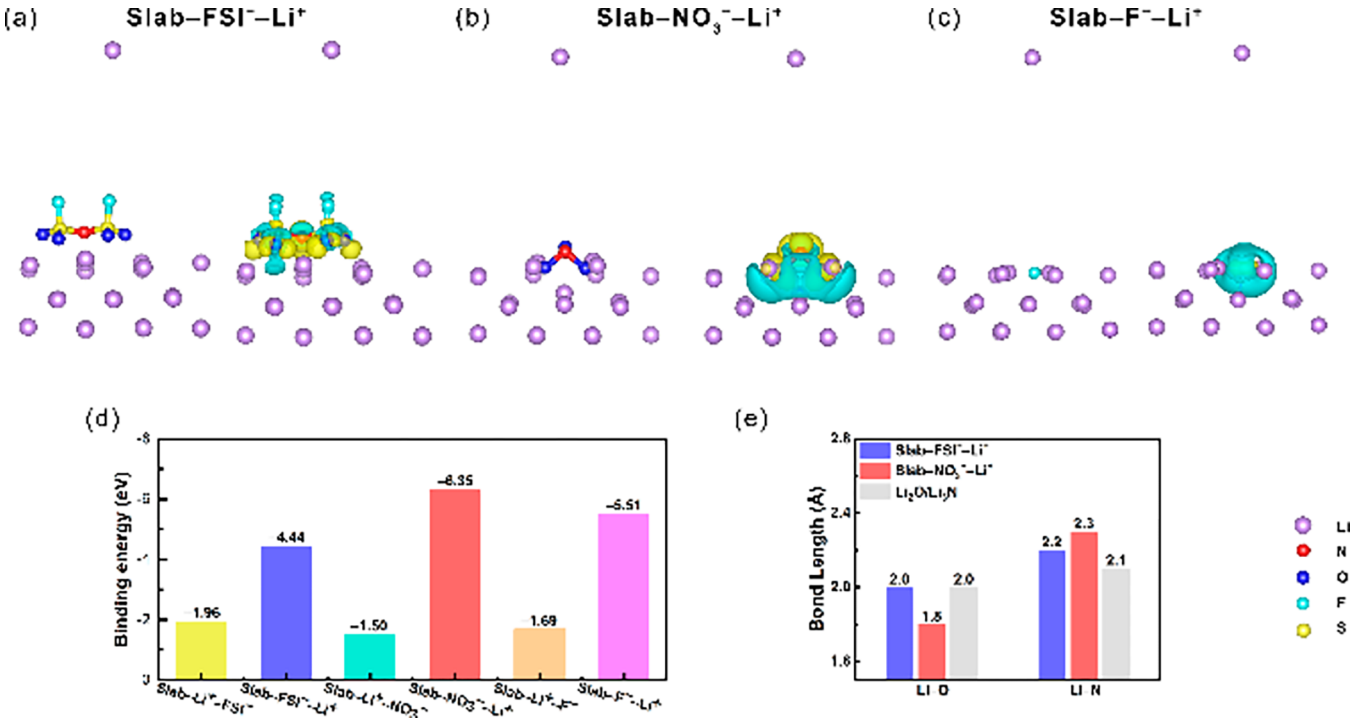

Figure 2. Optimized geometry and corresponding differential charge density distributions of (a) Slab−FSI^-−Li^+, (b) Slab−NO_3^-−Li^+, and (c) Slab−F^-−Li^+. Yellow represents the electron-accumulation area, while cyan is the electron-depletion area. The iso-surface level is 0.002. The lithium, nitrogen, oxygen, sulfur, and fluorine atoms are marked with purple, red, blue, yellow, and light blue, respectively. (d) The binding energies of the Slab−Li^+−A^- and Slab−A^-−Li^+ models. (e) The Li−O and Li−N bond lengths in Slab−FSI^-−Li^+ and Slab−NO_3^-−Li^+.

1.851 Å, which is slightly shorter than that in LiF (2.042 Å) crystals (Figure S8). The anions can even be reduced and decomposed on the Li slab in some conditions (Figure S9). Comparing with FSI^- and F^-, NO_3^- is of larger binding energy to the Li slab, indicating NO_3^- ions are the dominating ions in the IHP on Li metal anodes. The NO_3^--rich IHP is supposed to render a unique SEI on Li metal anodes and is therefore responsible for the improved battery performance, which is in accordance with previous reports that $LiNO_3$ is an excellent electrolyte additive for Li metal batteries.[32−34]

Faradaic and Non-Faradaic Processes. To further understand the non-Faradaic double layer capacitance adsorption process as well as the Faradaic decomposition process in the IHP, linear sweep voltammetry (LSV) at a range of 0−2.8 V versus Li/Li^+ was conducted (Figure 3a). The lithium foils were polished with tetrahydrofuran (THF) and washed with *n*-hexane. Scanning electron microscopy (SEM) and X-ray diffraction (XRD) images of treated lithium foils are given in Figure S10, exhibiting the smooth flat surface and pure lithium phase. The non-Faradaic process took place between 1.5 and 2.8 V. Alternating current (AC) voltammetry was further employed to record the adsorption behavior, and the capacitance of the adsorption was calculated by data achieved in AC voltammetry.[21] The potential of zero charge (PZC) describes the condition when the capacitance on a surface is minimum.[17] As indicated in Figure 3b, the value of the PZC shifted with the addition of $LiNO_3$ and CuF_2, reflecting the different adsorbed species in the IHP. When referring to the Faradaic process, the reduction potential of NF-LiFSI/DME electrolyte started at 1.5 V, indicating the preferential reduction of NO_3^-,[34] about 0.4 V earlier than the reduction of FSI^- in LiFSI/DME electrolyte. The additional reduction peak appearing at 0.6 V represents the underpotential deposition (UPD) of Li,[35] which occurs in the

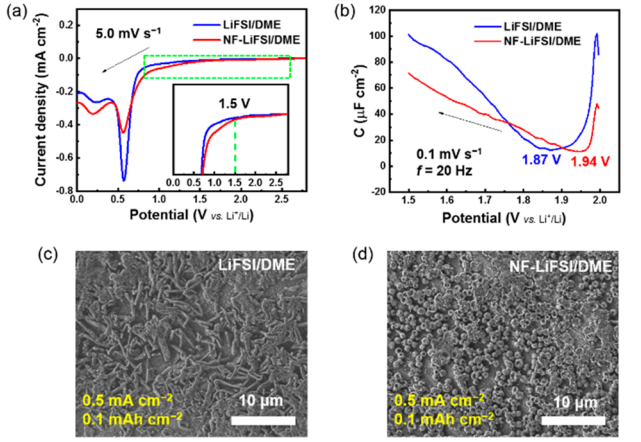

Figure 3. (a) The linear sweep voltammetry (LSV) curves of the LiFSI/DME and NF-LiFSI/DME electrolytes. (b) The non-Faradaic capacitance−potential curves for the copper electrode at 1.5−2.0 V (vs Li^+/Li). (c and d) SEM images of Li nucleation at the beginning deposition.

initial SEI formation. Meanwhile, a stripping process in LSV is delivered and two new peaks appeared at 1.9 and 2.4 V in NF-LiFSI/DME (Figure S11), indicating the reduction of new components in NF-LiFSI/DME induced SEI layer. In order to further exclude the influence when a tiny amount of water exists in electrolyte, 6000 ppm water is intentionally added in these electrolytes. Obviously different LSV lines are achieved (Figure S12) with the presence of water, indicating the reduction potential of 1.5 V is not contributed by water. Therefore, we conclude that the NO_3^- is not only preferentially adsorbed in the IHP rather than Li^+ and FSI^-, but it also reduced prior to them to initialize the formation of SEI film.

DOI: 10.1021/jacs.9b05029
J. Am. Chem. Soc. 2019, 141, 9422−9429

Mechanism Studies. The SEI layers induced by different IHPs unambiguously guide different morphologies of Li deposition (Figure 3c and d). Compared to the dendritic growth of Li in the FSI^--rich IHP induced SEI, the NO_3^--rich IHP induced SEI can guide the spherical growth of Li. The spherical nucleation morphology is preserved even at increased deposition capacities (Figure S13). Those results are well consistent with our previous report on plating morphologies of Li,[34] further confirming the component and structure of the SEI are closely dependent on the initial adsorption of the IHP in addition to the inner solvation sheath structure of Li^+ in bulk electrolyte. Therefore, the SEI will not only determine the Li deposition in thermodynamics but will also promote dynamics behaviors in a working battery.

The whole scenarios of Li^+ from the transport of solvation sheath structure in bulk electrolyte to the electric double layer capacitance on the electrode are undergoing cruel competition for adsorbing in IHP with NO_3^-, FSI^-, F^-, and DME solvents (Figure 4). We believe that both solvation Li^+ sheath structure

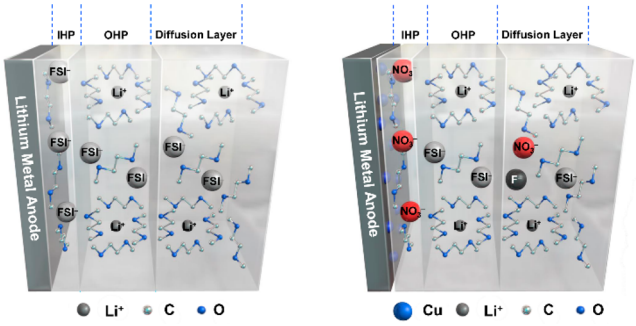

Figure 4. Schematic descriptions of a grim competitive journey of solvated Li^+ from bulk electrolyte to Li electrode (IHP stands for inner Helmholtz plane, OHP stands for outer Helmholtz plane).

and specific adsorption in IHP are crucial in SEI formation. As a result, a trace amount of Cu^{2+} cations is speculated to incorporate in the Li surface due to the thermodynamic replacement reaction with Li; meanwhile, NO_3^- anions are carried to IHP as the primary solvation sheath of Cu^{2+}, leading to the initial preferential decomposition in the formation of a Cu/nitride mixed conductor interphase layer.

The Cu atoms have been detected by X-ray photoelectric spectroscopy (XPS) after the first cycle in the NF-LiFSI/DME Li/Li battery (Figure S14a), whose peaks appear at 933.0 eV (2p 3/2) and 952.3 eV (2p 1/2), which are not detected for the Li metal surface in the LiFSI/DME electrolyte (Figure S15). Additionally, the signal of Cu is not found at the initial sputtering, indicating an electronic insulation film formed upon the layer of mixed conductor interphases. Therefore, the highly ionic conductive nitride interphases and domains are created by discrete Cu atoms, leading to the integrated feature of a protected film (Figure S14b). The result is in good accordance with the electrochemical performance of LFP|Li cells in 2.3 M LiFSI/DME with 20 mmol L^{-1} $LiNO_3$ or $Cu(NO_3)_2$ additive (Figure S5), further confirming the existence of Cu in the SEI layer will raise the stability of the lithium interface. The features of interfacial chemistry are preserved even after 100 cycles (Figure S14c), indicating the protected film can commendably sustain stress variation during repeated plating/stripping. The O 1s and N 1s in LiN_xO_y (binding energy at 530.8 and 398.2 eV, respectively), as an important composition of the SEI, which was induced by NO_3^-, kept still after 100 cycles in NF-LiFSI/DME (Figures S16 and S17). However, the O 1s and N 1s in $-N(SO_2)_2$ (binding energy at 532.1 and 397.5 eV, respectively) converted into Li_2O (529.0 eV) and −N−S (399.5 eV) during cycling (Figures S18 and S19). Therefore, the interfacial chemical evolution of O 1s (Figure S16) and N 1s (Figure S17) XPS depth profiles also demonstrates the indestructible feature compared to the fragile pristine SEI layer LiFSI/DME.

The structure of the SEI was characterized via scanning transmission electron microscopy (STEM). Figure 5a exhibited

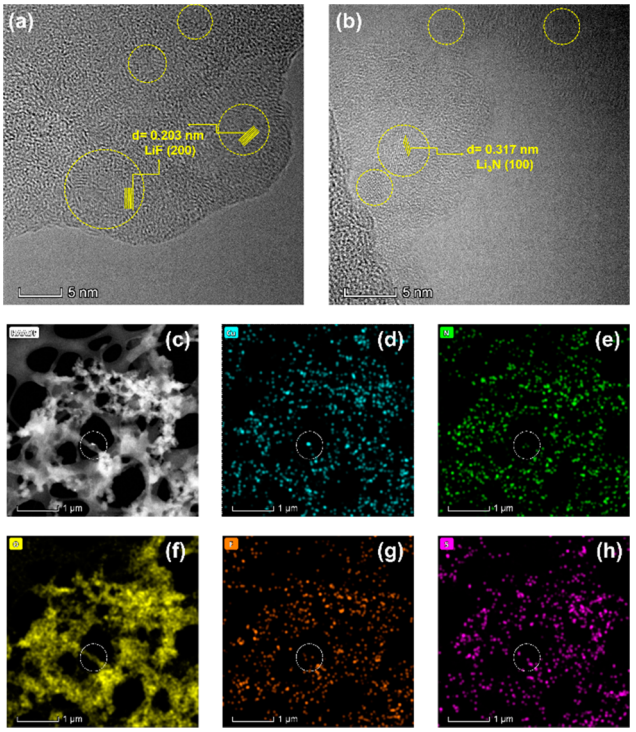

Figure 5. STEM study on the SEI structure. (a) The high resolution images of SEI formed in LiFSI/DME. The lattice spacing is 0.203 nm in circular areas, corresponding to the {200} planes of LiF. (b) The high resolution images were also given after the materials in the field of vision were in a stable condition. The lattice spacing is 0.317 nm in circular areas, corresponding to the {100} planes of Li_3N. (c−e) HAADF−STEM mapping of elemental Cu, N, O, F, and S.

the high resolution images of the SEI formed in LiFSI/DME, where the components in most regions were amorphous. According to the lattice fringe that was observed in the crystalline region (Figure 5a), the lattice spacing was 0.203 nm, corresponding to the {200} planes of LiF. The LiF was generated by the decomposition of FSI^-, which has been proved in previous reports.[9] Unfortunately, the NF-LiFSI/DME induced SEI cannot be captured due to its extremely unstable characteristics, and neither the amorphous nor crystalline was observed even after several attempts. What we can see was the melting and disappearing of certain materials (ja9b05029_si_002.mp4), possibly representing the irradiation damage of LiN_xO_y. A high resolution image was also given after the components in the field of vision were in a stable condition. The lattice spacing was 0.317 nm, corresponding to the {100} planes of Li_3N. Li_3N was generated from the reduction of LiN_xO_y under a high voltage of 60 kV. It is worth mentioning that LiF was not found in Figure 5b, confirming the absence of FSI^- and F^- in the initial IHP. The additional EDS of the SEI layer exhibited

DOI: 10.1021/jacs.9b05029
J. Am. Chem. Soc. 2019, 141, 9422−9429

consistent changes in the elements Cu, N, and O (circular areas in Figure 5c–f) but inconsistent changes with the elements F and S (circular areas in Figure 5g and h). Therefore, the NO_3^- induced SEI was strikingly different than the FSI^- induced SEI, further influencing the dynamics of Li^+.

Xu et al. claimed that the energy consumption of the Li^+ desolvation process is the main and rate-determining energy barrier in the migration of Li^+, referring to E_{a2}.[27] Although E_{a2} is independent of E_{a1}, it generates an apparent increase of ca. 20 kJ mol^{-1} with the presence of SEI. The SEI layer plays a crucial role in breaking the coordinated chemical forces between solvents and Li^+, determining the total value of E_{a2}. Mizuno et al. also identified both E_{a1} and E_{a2} as the activation energies related to OHP and IHP, IHP, and electrode ion diffusion, respectively.[18] Herein, we find the values of E_{a1} in two-electrolyte systems are slightly different, which is induced by the similar solvation in the OHP. In detail, the E_{a1} of NF-LiFSI/DME is slightly smaller than that of LiFSI/DME, mainly ascribed to the Cu–NO_3^- complex induced film renders the rapid across of Li^+ than FSI^- induced SEI layer. Both the higher ionic conductivity of the nitride interphase and more domains (Figure S14) can afford more ion channels, resulting in a smaller barrier for Li^+ to get through. However, there is a wide gap of E_{a2} between NF-LiFSI/DME and LiFSI/DME electrolytes. The E_{a2} of NF-LiFSI/DME is 48.1 kJ mol^{-1}, about one-third of that in LiFSI/DME. The energy barrier of the Li^+ desolvation process, or the so-called charge transfer process, is obviously reduced.

The different interfacial chemistry of the Li anode, including chemical composition and space structure, contributes to the significant difference of E_{a2}. The unique chemical compositions have been confirmed by XPS results (Figures S14–S19). The spectra of N 1s and Cu 2p exhibit a significant difference, indicating that the nitride interphase and the discrete Cu atoms can promote the desolvation of Li^+. Unfortunately, limited by the current experimental technique, another factor of space structure is tough to be probed except for STEM. According to our results and previous reports,[18,26,27] the initial OHP derived SEI of the Li anode mainly influences E_{a1}, while E_{a2} is determined by the initial IHP derived SEI (Figure 6). The gap between solvation Li^+ and the adsorbed species in the electric double layer about the electrode interface formation is perfectly filled at the nanoscale level. Regulating the adsorption species on the IHP and the primary solvation sheath structure is an important and effective strategy in exploring the thermodynamics and dynamics of Li^+ in a working battery.

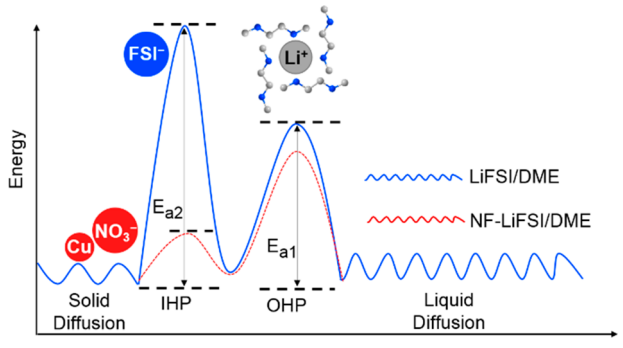

Figure 6. Correlation between the energy barrier of Li^+ and the specific adsorption in the inner Helmholtz plane (IHP) and outer Helmholtz plane (OHP). The initial OHP mainly influences E_{a1}, while E_{a2} is determined by the initial IHP.

There are three major related principles in regulating the species in the IHP. (i) Charge properties. When a lithium metal is brought into contact with a nonaqueous electrolyte, the anions in solution tend to lose part of their solvation shell to absorb directly at the closest surface, forming the inner Helmholtz plane. The inner Helmholtz plane on the Li metal anode has something in common with the IHP in the aqueous system where both emphasize the adsorption of anions.[36] (ii) Donor number (DN). DN is related to the electrostatic force between the anions and the lithium electrode. Anions with a high donor number will take a good advantage in entropic force and win the absorbed competition. Herein, in contrast to the FSI^- and DME with a low DN, NO_3^- with a high DN will preferentially absorb in the IHP. (iii) Spatial configuration. Despite that some anions have a chelated structure with the central cations and simultaneously possess a high donor number, the steric effect of some anions will dominate the weak adsorption ability in forming the IHP.

To further confirm the interfacial resistance of the Cu–NO_3^- complex induced film in the practical system, EIS of Li|LFP batteries have been collected. Compared to FSI^- induced SEI, series semicircles with a smaller diameter and more stable values are observed in Cu–NO_3^- induced film (Figure S20). The resistance hardly increases even after 700 cycles (Figure S21), indicating a lower energy barrier for Li^+ to cross the film. Additionally, the semicircles in middle frequency are too small to be detected for NF-LiFSI/DME, which can be considered almost absent, while the semicircles appear to be obvious in LiFSI/DME (Figure S21). Therefore, the high energy barrier for desolvation of Li^+ in LiFSI/DME eventually leads to the decomposition of DME as well as the failure of the Li|LFP battery.

In order to demonstrate this strategy in pouch cells, a 250 mAh pouch cell is assembled with LFP cathodes of an areal capacity of 2.0 mAh cm^{-2} and 50 μm thick Li foil as the anode. The pouch cell with NF-LiFSI/DME electrolyte delivered a capacity retention of 99.82% at 0.2 C after 80 cycles and a stable overpotential of electrochemical lithiation/delithiation within 80 cycles (Figure S22). The seamlessly integrated cycling performance between coin and pouch cells is attributed to the uniform and dense film formed on the Li anode.

CONCLUSION

In summary, there is fierce competition among the solvents, cations, and anions in nonaqueous electrolyte building the interface during the electrochemical process. Not only the solvation Li^+ in a working lithium metal cell but also the initial constitutions of the electric double layer that are covered on the electrode before cycling are very critical in achieving the initial SEI layer. Taking advantage of the rapid chemical replacement reaction, we employ Cu^{2+} as targetable anion and solvent carriers, guiding the NO_3^- to preferentially take part in the IHP. The SEI film formed with similar solvation Li^+ consumes the almost equivalent activation energy (E_{a1}) for Li^+ to get through the OHP. However, the charge transfer activation energy (E_{a2}), mainly the Li^+ desolvation process in the OHP and IHP derived film, gets a sharp reduction. Therefore, the interfacial chemistry and unique structure of the SEI are dependent on the adsorbed species in the IHP in addition to solvation Li^+, bridging the gap between adsorption and solvation in forming the electrode interface and completing the whole scenario about the journey from the bulk electrolyte to the Li metal anode.

DOI: 10.1021/jacs.9b05029
J. Am. Chem. Soc. 2019, 141, 9422–9429

■ ASSOCIATED CONTENT

Supporting Information

The Supporting Information is available free of charge on the ACS Publications website at DOI: 10.1021/jacs.9b05029.

NMR, voltage−time curves, electrochemical performance, optimized geometry, and bond analysis (PDF)

Video showing the melting and disappearing of certain materials, possibly representing the irradiation damage of LiN_xO_y (MP4)

■ AUTHOR INFORMATION

Corresponding Author

*jqhuang@bit.edu.cn

ORCID

Chong Yan: 0000-0001-9521-4981
Xiang Chen: 0000-0002-7686-6308
Xue-Qiang Zhang: 0000-0003-2856-1881
Xin-Bing Cheng: 0000-0001-7567-1210
Jia-Qi Huang: 0000-0001-7394-9186
Qiang Zhang: 0000-0002-3929-1541

Notes

The authors declare no competing financial interest.

■ ACKNOWLEDGMENTS

This work was supported by National Key Research and Development Program (2016YFA0202500 and 2016YFA0200102), National Natural Science Foundation of China (21776019, 21676160, 21825501, 21805161, and U1801257), and Tsinghua University Initiative Scientific Research Program. The authors acknowledge the support from Tsinghua National Laboratory for Information Science and Technology for theoretical simulations. The authors thank Hong-Jie Peng and Bo-Quan Li for useful discussions.

■ REFERENCES

(1) Manthiram, A.; Yu, X.; Wang, S. Lithium battery chemistries enabled by solid-state electrolytes. *Nat. Rev. Mater.* **2017**, *2* (4), 16103.

(2) Lin, D. C.; Liu, Y. Y.; Cui, Y. Reviving the lithium metal anode for high-energy batteries. *Nat. Nanotechnol.* **2017**, *12* (3), 194−206.

(3) Cheng, X. B.; Zhang, R.; Zhao, C. Z.; Zhang, Q. Toward Safe Lithium Metal Anode in Rechargeable Batteries: A Review. *Chem. Rev.* **2017**, *117* (15), 10403−10473.

(4) Zhang, S. S. Problem, Status, and Possible Solutions for Lithium Metal Anode of Rechargeable Batteries. *ACS Appl. Energy Mater.* **2018**, *1* (3), 910−920.

(5) Li, Y.; Li, Y.; Pei, A.; Yan, K.; Sun, Y.; Wu, C. L.; Joubert, L. M.; Chin, R.; Koh, A. L.; Yu, Y.; Perrino, J.; Butz, B.; Chu, S.; Cui, Y. Atomic structure of sensitive battery materials and interfaces revealed by cryo-electron microscopy. *Science* **2017**, *358* (6362), 506−510.

(6) Cheng, X.-B.; Yan, C.; Chen, X.; Guan, C.; Huang, J.-Q.; Peng, H.-J.; Zhang, R.; Yang, S.-T.; Zhang, Q. Implantable Solid Electrolyte Interphase in Lithium-Metal Batteries. *Chem.* **2017**, *2* (2), 258−270.

(7) Tu, Z.; Choudhury, S.; Zachman, M. J.; Wei, S.; Zhang, K.; Kourkoutis, L. F.; Archer, L. A. Designing Artificial Solid-Electrolyte Interphases for Single-Ion and High-Efficiency Transport in Batteries. *Joule* **2017**, *1* (2), 394−406.

(8) Suo, L.; Borodin, O.; Gao, T.; Olguin, M.; Ho, J.; Fan, X.; Luo, C.; Wang, C.; Xu, K. Water-in-salt" electrolyte enables high-voltage aqueous lithium-ion chemistries. *Science* **2015**, *350* (6263), 938−943.

(9) Yamada, Y.; Furukawa, K.; Sodeyama, K.; Kikuchi, K.; Yaegashi, M.; Tateyama, Y.; Yamada, A. Unusual stability of acetonitrile-based superconcentrated electrolytes for fast-charging lithium-ion batteries. *J. Am. Chem. Soc.* **2014**, *136* (13), 5039−5046.

(10) Fan, X.; Chen, L.; Borodin, O.; Ji, X.; Chen, J.; Hou, S.; Deng, T.; Zheng, J.; Yang, C.; Liou, S.-C.; Amine, K.; Xu, K.; Wang, C. Non-flammable electrolyte enables Li-metal batteries with aggressive cathode chemistries. *Nat. Nanotechnol.* **2018**, *13* (8), 715−722.

(11) Qian, J.; Henderson, W. A.; Xu, W.; Bhattacharya, P.; Engelhard, M.; Borodin, O.; Zhang, J. G. High rate and stable cycling of lithium metal anode. *Nat. Commun.* **2015**, *6*, 6362.

(12) Xu, K.; Lam, Y.; Zhang, S. S.; Jow, T. R.; Curtis, T. B. Solvation Sheath of Li^+ in Nonaqueous Electrolytes and Its Implication of Graphite/Electrolyte Interface Chemistry. *J. Phys. Chem. C* **2007**, *111* (20), 7411−7421.

(13) Bogle, X.; Vazquez, R.; Greenbaum, S.; Cresce, A.; Xu, K. Understanding Li^+−Solvent Interaction in Nonaqueous Carbonate Electrolytes with ^{17}O NMR. *J. Phys. Chem. Lett.* **2013**, *4* (10), 1664−1668.

(14) Zhang, X.-Q.; Chen, X.; Cheng, X.-B.; Li, B. Q.; Shen, X.; Yan, C.; Huang, J.-Q.; Zhang, Q. Highly Stable Lithium Metal Batteries Enabled by Regulating the Solvation of Lithium Ions in Nonaqueous Electrolytes. *Angew. Chem., Int. Ed.* **2018**, *57* (19), 5301−5305.

(15) Kim, H. M.; Hwang, J.-Y.; Aurbach, D.; Sun, Y.-K. Electrochemical Properties of Sulfurized-Polyacrylonitrile Cathode for Lithium-Sulfur Batteries: Effect of Polyacrylic Acid Binder and Fluoroethylene Carbonate Additive. *J. Phys. Chem. Lett.* **2017**, *8* (21), 5331−5337.

(16) Valette, G.; Parsons, R. Adsorption on well-defined solid surfaces: Bromide adsorption on a (110) face of silver. *J. Electroanal. Chem. Interfacial Electrochem.* **1985**, *191* (2), 377−386.

(17) Valette, G. Inner-layer capacity at the PZC for perfect (111), (100) and (100) faces of silver: Surface area and capacitance contributions of superficial defects for real electrodes. *J. Electroanal. Chem. Interfacial Electrochem.* **1987**, *224* (1), 285−294.

(18) Mizuno, Y.; Okubo, M.; Asakura, D.; Saito, T.; Hosono, E.; Saito, Y.; Oh-ishi, K.; Kudo, T.; Zhou, H. Impedance spectroscopic study on interfacial ion transfers in cyanide-bridged coordination polymer electrode with organic electrolyte. *Electrochim. Acta* **2012**, *63*, 139−145.

(19) Wang, F.; Borodin, O.; Ding, M. S.; Gobet, M.; Vatamanu, J.; Fan, X. L.; Gao, T.; Edison, N.; Liang, Y. J.; Sun, W.; Greenbaum, S.; Xu, K.; Wang, C. S. Hybrid Aqueous/Non-aqueous Electrolyte for Safe and High-Energy Li-Ion Batteries. *Joule* **2018**, *2* (5), 927−937.

(20) Yang, C.; Chen, J.; Qing, T.; Fan, X.; Sun, W.; von Cresce, A.; Ding, M. S.; Borodin, O.; Vatamanu, J.; Schroeder, M. A.; Eidson, N.; Wang, C.; Xu, K. 4.0 V Aqueous Li-Ion Batteries. *Joule* **2017**, *1* (1), 122−132.

(21) Herzog, G.; Moujahid, W.; Strutwolf, J.; Arrigan, D. W. Interactions of proteins with small ionised molecules: electrochemical adsorption and facilitated ion transfer voltammetry of haemoglobin at the liquid/liquid interface. *Analyst* **2009**, *134* (8), 1608−1613.

(22) Kresse, G.; Furthmüller, J. Efficient iterative schemes for ab initio total-energy calculations using a plane-wave basis set. *Phys. Rev. B: Condens. Matter Mater. Phys.* **1996**, *54* (16), 11169−11186.

(23) Hohenberg, P.; Kohn, W. Inhomogeneous Electron Gas. *Phys. Rev.* **1964**, *136* (3B), B864−B871.

(24) Kresse, G.; Furthmüller, J. Efficiency of ab-initio total energy calculations for metals and semiconductors using a plane-wave basis set. *Comput. Mater. Sci.* **1996**, *6* (1), 15−50.

(25) Perdew, J. P.; Burke, K.; Ernzerhof, M. Generalized Gradient Approximation Made Simple. *Phys. Rev. Lett.* **1996**, *77* (18), 3865−3868.

(26) Abe, T.; Fukuda, H.; Iriyama, Y.; Ogumi, Z. Solvated Li-Ion Transfer at Interface Between Graphite and Electrolyte. *J. Electrochem. Soc.* **2004**, *151* (8), A1120−A1123.

(27) Xu, K.; von Cresce, A.; Lee, U. Differentiating Contributions to "Ion Transfer" Barrier from Interphasial Resistance and Li^+ Desolvation at Electrolyte/Graphite Interface. *Langmuir* **2010**, *26* (13), 11538−11543.

(28) Zhang, L. L.; Zhao, X. S. Carbon-based materials as supercapacitor electrodes. *Chem. Soc. Rev.* **2009**, *38* (9), 2520−2531.

(29) Valette, G. Double layer on silver single crystal electrodes in contact with electrolytes having anions which are slightly specifically

DOI: 10.1021/jacs.9b05029
J. Am. Chem. Soc. 2019, 141, 9422−9429

adsorbed. *J. Electroanal. Chem. Interfacial Electrochem.* **1982**, *138* (1), 37−54.
(30) Valette, G. Double layer on silver single crystal electrodes in contact with electrolytes having anions which are slightly specifically adsorbed: Part III. The (111) face. *J. Electroanal. Chem. Interfacial Electrochem.* **1989**, *269* (1), 191−203.
(31) Ding, M.; Zhong, G.; Zhao, Z.; Huang, Z.; Li, M.; Shiu, H. Y.; Liu, Y.; Shakir, I.; Huang, Y.; Duan, X. On-Chip in Situ Monitoring of Competitive Interfacial Anionic Chemisorption as a Descriptor for Oxygen Reduction Kinetics. *ACS Cent. Sci.* **2018**, *4* (5), 590−599.
(32) Guo, J.; Yang, Z.; Yu, Y.; Abruña, H. D.; Archer, L. A. Lithium−Sulfur Battery Cathode Enabled by Lithium−Nitrile Interaction. *J. Am. Chem. Soc.* **2013**, *135* (2), 763−767.
(33) Burke, C. M.; Pande, V.; Khetan, A.; Viswanathan, V.; McCloskey, B. D. Enhancing electrochemical intermediate solvation through electrolyte anion selection to increase nonaqueous Li-O_2 battery capacity. *Proc. Natl. Acad. Sci. U. S. A.* **2015**, *112* (30), 9293−9298.
(34) Yan, C.; Yao, Y. X.; Chen, X.; Cheng, X. B.; Zhang, X. Q.; Huang, J. Q.; Zhang, Q. Lithium Nitrate Solvation Chemistry in Carbonate Electrolyte Sustains High-Voltage Lithium Metal Batteries. *Angew. Chem., Int. Ed.* **2018**, *57* (43), 14055−14059.
(35) Aurbach, D. The Electrochemical Behavior of Lithium Salt Solutions of γ-Butyrolactone with Noble Metal Electrodes. *J. Electrochem. Soc.* **1989**, *136* (4), 906−913.
(36) Borodin, O.; Ren, X.; Vatamanu, J.; von Wald Cresce, A.; Knap, J.; Xu, K. Modeling Insight into Battery Electrolyte Electrochemical Stability and Interfacial Structure. *Acc. Chem. Res.* **2017**, *50* (12), 2886−2894.

DOI: 10.1021/jacs.9b05029
J. Am. Chem. Soc. 2019, 141, 9422−9429